LBL--13727

DE82 005652

Meson Production in Relativistic-Heavy-Ion Collisions

Stephen R. Schnetzer
(Ph.D. thesis)

Nuclear Science Division
Lawrence Berkeley Laboratory
University of California
Berkeley, CA 94720

August 1981

This work was supported by the Director, Office of Energy Research Division of Nuclear Physics of the Office of High Energy and Nuclear Physics of the U.S. Department of Energy under Contract W-7405-ENG-48.

Meson Production in Relativistic Heavy Ion Collisions

Stephen R. Schnetzer

ABSTRACT

We have measured the inclusive K^+ production cross sections at angles from 15° to 80° in collisions of protons (2.1 GeV) and deuterons (2.1 GeV/amu) on NaF and Pb, and Ne (2.1 GeV/amu) on C, NaF, KCl, Cu, and Pb. The kaons were identified by measuring the time of flight and the momentum in a magnetic spectrometer, and by detecting the particles from the kaon decays in a Pb glass Cerenkov counter. The momentum range of the detected kaons extended from 350 MeV/c to 750 MeV/c. The multiplicity of each event was measured by a set of scintillation counter telescopes which were situated around the target.

The differential cross section of the kaons falls off exponentially with center of mass energy in the nucleon nucleon center of mass frame. In addition, the angular distribution of the kaons is nearly isotropic in this frame even for p+NaF and Ne+Pb collisions.

The data are compared with a row on row model and a thermal model. Neither are able to explain all features of the data. The row on row model does not reproduce the near isotropy in the nucleon nucleon frame, and the thermal model overpredicts the kaon yield by a factor of approximately twenty.

Analysis of the A dependence shows that the increase in the cross section for kaon production between Ne+NaF and Ne+Pb collisions is greater than that between d+Naf and d+Pb. This may be an indication

of a collective effect.

In Ne+Pb collisions the associated multiplicity is approximately 10% higher when a kaon is detected in the spectrometer than when a proton or pion is detected. This indicates that the kaons may come from more central collisions.

ACKNOWLEDGEMENTS

One of the joys of this type of research is that it is a group effort and allows one the chance of working with some very great people. I would like to express my appreciation to these people here. Although they are allotted only one page of this thesis, they deserve a whole lot more.

Xixang Bai

Raymond Fuzesy

Hideki Hamagaki

Seiji Kadota

Marie-Claude Lemaire

Roselyne Lombard

Yasuo Miake

Jeanne Miller

Eckhard Moeller

Shoji Nagamiya

Gilbert Shapiro

Isao Tanihata

My thesis adviser, Prof. Herbert Steiner, deserves special mention. Needless to say, he deserves most of the credit for seeing me through these, at times, troubled waters.

TABLE OF CONTENTS

I. Introduction 1

1. Experimental 1

2. Theoretical 1

2.1 Motivation 1

2.2 Abnormal States 3

2.3 Uniqueness of Kaons 5

2.4 Model Descriptions 7

2.4.1 Thermal Models 8

2.4.2 Cascade (Row-On-Row) Models 11

2.4.3 Hydrodynamical Models 14

II. Experimental Methods 16

1. Beam 16

2. Targets 16

3. Intensity Monitoring 17

4. *Particle Detection* 17

4.1 Magnetic Spectrometer 17

4.1.1 Scintillation Counters 17

4.1.2 Bending Magnet 18

4.1.3 Wire Chambers 19

4.1.4 Lucite Cerenkov Counter 20

4.1.5 Lead-Glass Blocks 21

4.1.6 MATRIX 22

4.1.7 MBD 23

4.2 Scintillation Counter Telescopes 23

4.3 Trigger Logic and Electronics 24

4.4 Data Analysis 24

4.4.1 Efficiency Corrections 25

4.4.2 Track Reconstruction 26

4.4.3 Decay of Kaon in Flight 28

4.4.4 Invariant Cross Section 28

4.5 Sources of Error 29

III. Results 30

1. Model Comparisons 30

1.1 Row-On-Row Models 30

1.2 Thermal Models 32

2. Comparison of pp, pA, and AA Collisions 34

3. A - Dependences 36

4. Relative Cross Section for pp, pn, and nn 38

5. Total Cross Sections 40

6. Multiplicity 41

7. Conclusions 44

IV. References 57

V Figure Captions 60

VI. Appendices 92

A. Ionization Chamber Calibration 92

B. Trigger Electronics 93

C. Cross Section Tables 96

CHAPTER 1

INTRODUCTION

1. Experimental

In this thesis an experiment to measure kaon production in relativistic heavy ion collisions is described. The inclusive spectra of K^+ mesons in collisions of 2.1 GeV/amu nuclei with various targets were measured by means of a magnetic spectrometer. This spectrometer was rotated between laboratory angles of 15° and 80°. The momentum range of the detected kaons extended from 350 MeV/c to 750 MeV/c. In addition, the associated multiplicity of each event was measured by 16 scintillation counter telescopes which were situated around the target. The purpose of the experiment was to learn something new about the reaction mechanism of these collisons by studying a particle heretofore undetected in these collisions, namely K^+ mesons.

2. Theoretical

2.1. Motivation

The main interest in relativistic nuclear collisons arises because they may provide a means of studying nuclear matter under abnormal conditions of density and temperature. This idea is basically a very intuitive one. If we think of the nuclei as composite systems with collective modes of behavior, then, when we violently collide them together, we expect that they will undergo correspondingly violent disturbances. Specifically, we expect the nuclei somehow to compress

one another somewhat in analogy to colliding rubber balls. However, when the collisions are examined in light of what is currently known about nuclear physics, it remains uncertain as to whether significant compressions do actually occur. Nevertheless, the theoretical speculations are sufficiently interesting that an experimental search for evidence of this compression should be made.

The most intriguing of the theoretical speculations maintain that shock waves may be set up during the collisions.[1,2] This is argued from the fact that at projectile energies of a few hundred MeV/amu the velocity of the projectile will be greater than the speed of sound, $\approx c/3$, inside nuclear matter[3]. These shock waves might then lead to extremely high density pile-ups which could be more than 10 times normal density.[4,5] However, this picture is probably correct only if the hydrodynamic approximation[6] is valid. This approximation, which treats the nuclei as interacting fluids, is rigorously valid only if the nucleon mean free path for interaction is much less than the size of the system. For finite nuclei this is not the case, and several experiments which have been designed to search for shock waves have not found any conclusive evidence for their existence. This may be due, however, to the fact that detection of more than just a single particle must be made. Such experiments will be conducted in the near future.

Even if shock waves are not produced it may still be argued that densities up to about 3-4 times normal may be achieved.[7,8] Most of these speculations, also, depend upon the hydrodynamical approximation. They assume that local equilibrium is attained during the collision and that, therefore, the system can be described by an equation of state.

This equation in conjunction with the equations of fluid dynamics is then solved for the compressional energy and density. No great reliability can be attributed to these calculations, however, since little is known about the form to assume for the equation of state. In addition, it is possible that, at these energies, there may be a large amount of transparency with no equilibration.

Obviously it is of primary importance to ascertain experimentally how much compression, if any, does occur. Much effort is currently being expended to find the answer. This experiment is a part of this endeavor. It cannot provide a complete answer, but, because of its presently unique features, it should help to resolve some of the ambiguities.

2.2. Abnormal States

If large compressions do occur, then the exciting possibility exists that new states of nuclear matter may be discovered. These investigations are centered around gaining an understanding of the behavior of the nuclear equation of state. This equation gives the energy per nucleon as a function of density and temperature. The only things currently known about this equation is that the normal density is $\rho = 0.145\ fm^{-3}$ and that the energy per nucleon at this point is -15.960 MeV. Even the second derivative at this stable point which is related to the compressibility is unknown. As mentioned above, this is one of the reasons why it is very difficult to predict what will occur during the collisions. Therefore, even if no new states are discovered, any information which can be obtained about the parameters of this equation will contribute to our understanding of the nature of the nuclear force.

On the other hand, there are theoretical speculations which indicate that things might be much more exciting. Specifically, there are predictions that, at densities several times normal, nuclear matter may undergo phase transitions.

One possibility for which there have been several theoretical calculations is the transition to a pion condensate state.[9,10] As the nuclear density is increased the energy of particle-hole excitation states which have the quantum numbers of the pion, $J^P=0^-$, decreases and may become zero at some critical density, ρ_{cr}. Since these particle-hole states behave like bosons and, at the critical density, ρ_{cr}, could be produced at no energy cost, these quasi-particles should then condense out of the vacuum. This represents a phase transition of nuclear matter from its normal "liquid" state to a "spin-isospin lattice".[11] It would probably be a second order phase transition and would manifest itself as a shoulder in a plot of the equation of state. There has not been complete agreement among the calculations as to the value of ρ_{cr}. However, a value of 2-3 times normal seems to be favored. Unfortunately, most of the calculations are for infinite nuclear matter at zero temperature. The finite size effects and the large excitation energies necessarily involved in the compression add many complications and may even inhibit the transition from occuring. Also, even if the condensate exists experimental detection may be extremely difficult. Indeed, theorists have had difficulty in agreeing on a signature. They do agree however that the condensate will not lead to copious production of real pions in the laboratory.

Another speculation is that at sufficiently high densities the nucleons will lose their individual identities. Due to asymptotic freedom the quarks may act like free particles, and the nuclear matter may become a free quark gas.[12] Calculations based on the MIT bag model have shown that the energy density of this quark phase should vary with mass density, ρ, as $\rho^{1/3}$.[13] On the other hand, calculations for baryon matter show a dependence linear with ρ. Once again the critical density at which the transition occurs is model dependent but seems to be ≈ 10 times normal.

In addition to its interest from a purely nuclear physics viewpoint, this behavior of nuclear matter is extremely important for astrophysics and cosmology. The density in the center of neutron stars is expected to be 3 to 4 times normal density.[14] Therefore, if they exist at these densities, pion condensation and quark matter may have important consequences for the properties of these highly compressed, stellar objects. It is also important to know what happened in the early universe which, according to present big bang theories, was extremely dense and hot.[14] Relativistic, nuclear collisions probably provide the only means of simulating these conditions in the laboratory.

2.3. Uniqueness of Kaons

Before making comparisons to models we wish to describe the important features of the present experiment. The K^+ meson is distinguished from the other particles previously detected in heavy ion collisions in that it has the quantum number of positive strangeness. Since there are no known positive strangeness baryons the K^+ does not resonantly scatter with nucleons. Partly for this reason the K^+ has a

small cross section for scattering and undergoes almost no absorption. Quantitatively, the K^+N cross section is less than 13mb for a kaon with momentum less than 1 GeV/c.[15] Thus, the mean free path is ≥5fm. This means that the kaons will tend to travel directly from their point of production to the detector. Nucleons and pions, on the other hand, may undergo several collisions and, in the case of pions, be absorbed before they escape from the nuclear material. For this reason kaons may be more reliable harbingers of the early, perhaps highly compressed and very hot, stage of the reaction. Unfortunately, however, all may not be this straight forward. Due to the K^* resonance, the $K^+\pi$ cross section at energies of a few hundred MeV is relatively quite large.[16] Thus, if there are real pions present in the interaction zone the kaons may have a high probability to interact with them before getting out.

Another important feature of kaons is that they can only be produced in NN interactions via a three-body final state

$$N + N \rightarrow N + Y + K^+$$

where Y is a baryon with negative strangeness. This fact, along with the relatively large K^+ mass, 494 MeV, means that the threshold for K^+ production is much higher than for pions. The highest Bevalac energy of 2.1 GeV/amu, the energy at which this experiment was run, corresponds to a center of mass energy for free NN collisions of 2.73 GeV. If we ignore Fermi motion, then the allowed processes are:

1) $NN \rightarrow N\Lambda K^+$ 2) $NN \rightarrow N\Sigma K^+$

The threshold center of mass energy for 1) is 2.55 GeV while that for 2) is 2.62 GeV. Since a laboratory kinetic energy of 2.1 GeV/amu is only slightly above these thresholds, these reactions have very small

cross sections. In addition, for free NN collisions the spectra can be explained very well by simple phase space considerations.[17] Shown in Fig. 1 is a plot of total cross section as a function of P_{LAB} for the reactions $pp \rightarrow p\Lambda K^+$ and $pp \rightarrow p\Sigma^0 K^+$. In Fig. 2 is shown the K^+ spectra for $pp \rightarrow K^+X$ for a proton kinetic energy of 2.54 GeV. Even though this energy is somewhat above the Bevalac energy of 2.1 GeV/amu, it can be seen that phase space still gives a very good fit to the data. These two facts:

1) K^+ production is small

2) spectral shapes are explained by phase space

mean that abnormalities may show up more clearly in these spectra than in those for other particles.

Another caveat which should be observed here, however, is the fact that the K's can be produced via the interaction $\pi N \rightarrow K^+X$. This interaction has a relatively large cross section. It may, however, be argued that most of the π's come from decay of Δ's which, due to Lorentz time dilation, often does not occur until the Δ's are outside of the reaction region. Nevertheless, this is clearly a phenomenon which must be studied.

2.4. Model Descriptions

Since theory has not been able to indicate what the experimental signatures of phase transitions mentioned in sec. 2.2 are, the search for them is extremely complicated and ambiguous. Therefore, before much effort is expended in what may be a futile search, we must first try to discover whether the search is justified. That is, we should learn whether the large compressions needed to achieve these densities

actually do occur. To this end, we must study the reaction mechanism, that is, how the parameters of the system change during the collision. A large number of models have been proposed to describe this behavior. It would be tedious to describe all or even a large fraction of these. However, based upon their underlying assumptions it is possible to catagorize these models into several distinct groups. Below, therefore, we shall examine the features of each of three groups which seem to be the most important or are, at least, the most relevant in terms of the experiment we are describing here. We do this primarily by comparing with the existing data for proton and pion inclusive spectra in Ne+NaF collisions at 2.1 GeV/amu. The three types of models discussed are: thermal, cascade, and hydrodynamics. We also discuss what we may additionally learn about each of these models by means of the K^+ spectra measured in this experiment. We outline here only the possibilities which may exist. In Chapter 3 the actual data are presented and used to answer some of the questions which are posed here.

Since this experiment was carried out entirely at an energy of 2.1 GeV/amu we concentrate on a comparison of the models with data at this energy. One of the banes of relativistic heavy ion research is that an extremely large number of parameters is involved. These include: target and projectile mass, projectile energy, fragment detected, associated multiplicity, etc. Perhaps by narrowing our scope we can learn more and become less confused.

2.4.1. Thermal Models

The thermal or fireball models are perhaps the most intuitively simple and were among the first to give reasonable agreement with data.

The original fireball model[18,19] contained three important assumptions. First, in a given collision it assumed that the nucleons from the parts of the target and projectile which overlaped formed a system called the participant piece. It further assumed that this participant piece became completely thermalized, and that it had the properties of an ideal gas. It could be therefore characterized by a temperature, T, which for the non-relativistic case is given by $kT=\frac{2}{3}\eta(1-\eta)\epsilon$, where η = (number of participant nucleons from the projectile)/(total number of participants), and ϵ is the the kinetic energy per nucleon of the projectile nucleus. In the laboratory the fireball must move with a velocity, β, in order to conserve momentum. Nonrelativistically, this β is simply given by the kinematics to be. $\beta=\eta\beta_{beam}$. Finally, since there is no containing pressure the fireball freely expands. This leads to a momentum distribution in its center of mass which non-relativistically is the Maxwell-Boltzman distribution.

$$\frac{d^2N}{p^2dpd\Omega} = N(2\pi mkT)^{-3/2}e^{-p^2/2mkT}$$

To obtain the laboratory distribution then, one simply Lorentz transforms to a system moving with the velocity, β. Both β and T will depend upon the ratio of the number of projectile-contributed nucleons to the number of target-contributed ones which, in turn, depends upon the impact parameter. Since, generally, the experiments are not able to select the impact parameter, the measured spectra must be obtained by integration.

For the case of kaon production it is important to be able to incorporate particle production into the model. This is achieved by assuming that the different species of hadrons wihtin the fireball are in

chemical equilibrium.[20] The momentum distribution of a particle of type i is then given by

$$\frac{d^3N_i}{dp^3} = \frac{(2s_i+1)V}{(2\pi)^3}\left[\exp\left[\frac{m+T_{CM}-\mu_i}{k}T\right]\pm 1\right]^{-1}$$

Here s_i is the spin and μ_i is the chemical potential of particle type i. V is the volume at which the fireball freezes out. That is, it is the volume of the system when the density has become low enough so that the particles may be considered to be no longer interacting. The ± 1 refers to fermions and bosons respectively. There are 5 unknowns: the proton, neutron and kaon chemical potentials, the temperature and the freeze-out volume but there are also 5 conservation equations which are to be solved:

$$E = \sum_i N_i E_i \qquad Q = \sum_i N_i Q_i \qquad B = \sum_i N_i B_i$$

$$0 = \sum_i N_i S_i \qquad \rho_c = \frac{1}{V}\sum_i N_i$$

where E=energy, Q=charge, B=baryon number, S=strangeness, and ρ_c=freeze-out density.

The fireball model is somewhat unsatisfying in that the assumption of thermalization is very ad hoc. No macroscopic description of how the thermalization occurs is offered. Also, if the fireball model is essentially correct with all of the particles in thermal and chemical equilibrium, then even if phase transitions occur it will be very difficult to learn about them since the emitted particles will be thermalized before they are detected. Nevertheless, it is of course important to determine how much truth there actually is in the model.

Since the thermal models deal solely with contributions from the participant region, we concentrate for purposes of comparison upon

data[21] at 90° in the center of mass. Here contributions from the projectile and target spectators are expected to be small. Shown in Fig. 3 is a plot of invariant cross sections for protons and pions versus center of mass energy in collisions of 2.1 GeV/amu Ne+NaF. One thing that is immediately obvious is that both spectra have an exponential shape as the thermal models demand. However, the slopes for the protons and pions are different. If there is a unique freeze-out density for for both protons and pions, and if both types of particles are in chemical and thermal equilibrium, then we expect the slopes to be equal. Since, however, the mean free path of nucleons in this energy range is generally larger than that of pions, $\lambda_{NN} \approx 2f$ while $\lambda_{\pi N} \approx .5\text{-}2f$, it may be that the NN interactions decouple before the πN interactions do. This would lead to a larger freeze-out density and thus higher temperature and a less steep slope for the nucleons. If this picture is correct, then, since the KN cross section is even smaller, the K's should freeze-out even sooner and have a still higher temperature.

2.4.2. Cascade (Row-On-Row) Models

The cascade model[22,23,24] approach is philosophically radically different from that of the thermal models since no equation of state is assumed. Instead, the nuclear collision is treated from an entirely microscopic viewpoint. That is, the collision is assumed to be made up of a superposition of individual, binary interactions. The history of each particle is treated by Monte Carlo methods with the probability of scattering on another particle given by the free particle cross sections. Between collisions the particles travel on straight line trajectories. All phase correlations between nucleons are neglected.

If the nuclei behaved classically like bags of marbles, and if the calculation is sufficiently complete to accurately trace out the evolution of all of the particles then agreement with experiment is expected. Any disagreement between the calculation and the data necessarily implies either that the assumptions of the model are incorrect or that the approximations used in the calculations are too simple or both. The uncertainties arise in trying to incorporate quantum mechanics and the effects of the nuclear environment. Specifically, Fermi motion, the Pauli principle, and pion and resonance production must be treated. The treatment of each of these effects can, as yet, only be approximate, and each leads to some difficulty.

Since the cascade codes assume that the individual nucleon collisions occur in isolation, they cannot be used to predict the onset of phase transitions. It is, nevertheless, interesting to examine whether compression still occurs in these models. In fact, in a recent model, densities considerably larger than 2 times normal occur.[23] Therefore, even though cascade models do not incorporate phase transitions, they may be able to describe the collision process up to the point of the transition. A test of their validity is therefore important. Since phase transitions probably occur, if at all, in only a small fraction of the events, the large majority of the events may be used to test the cascade calculations.

The row-on-row models[25] are a subset of the cascade models. They reduce the full three-dimensional cascade problem to one dimension by assuming that one row of nucleons in the projectile scatters off of only one row of nucleons in the target. This

approximation becomes more valid at higher energies since there the NN cross sections become more forwardly peaked. Obviously this type of model cannot be more valid than a full scale cascade calculation. Its main virtue is that the complexity of the computer code is considerably reduced. The reason that we introduce it here is that, currently, the most extensive calculation which has been done for kaon production is based on this model.[26] Ideally we would wish to compare our results with the full three-dimensional cascade codes, but, unfortunately, incorporating kaon production into these codes is a large task which must be left to the future.

Fig. 4 shows a comparison of a row-on-row calculation[26] with the measured proton inclusive spectra[21] for collisions of 2.1 GeV/amu Ne on NaF and Pb. It can be seen that the agreement is at best fair. It is argued that this discrepancy may be accounted for by the fact that Δ production has not been incorporated in this particular calculation. Since, however, Δ's probably do not play a significant role in the production of kaons, this may not be a serious flaw in the ability to predict the kaon spectra.

As mentioned, one of the interesting features of the K's is their ability to reach the detector relatively unperturbed. It is, therefore, important to know what the probability of rescattering actually is. This particular row-on-row calculation allows a certain amount of rescattering to be built in.[27] It can, therefore, be used to test how much rescattering is required to best fit the K^+ spectra. As outlined above, we may imagine that most events are unexotic and may be reasonably described by this simple model. If, in the future, a means of triggering

on the more exotic events is found, and if kaon detection is to be used as a probe, then a knowledge of this rescattering will be extremely important.

2.4.3. Hydrodynamical Models

The last class of models that we discuss are those based on hydrodynamics.[28,29] As mentioned previously, these models are based on the assumption that the mean free path for interaction is much less than the size of the system. Since the transparency of the nuclei increases with increasing energy, these models should work best at relatively low, bombarding energies. Indeed, these calculations are usually compared with data at an incident energy of 400 MeV/amu or less. This experiment, however, was performed exclusively at an energy of 2.1 GeV/amu. Nevertheless, coherent or collective effects may arise which might cause the effective NN mean free path to be short enough even at these energies. Since, at present, the hydrodynamic models provide perhaps the only means of studying the nuclear equation of state, the comparison, even at these energies, is extremely worthwhile.

Generally these models consider two nuclear fluids, the target and the projectile. The behavior of each of these fluids is determined by the fluid dynamic conservation equations for nucleon number, momentum, and energy. In addition, terms are introduced into these equations to allow for a coupling of the two fluids by means of energy and momentum transfer. In addition, the equation of state is used to obtain a relationship between the pressure and the energy density.

The goal, then, is to fit the data by selecting an appropriate form for the equation of state. Of course, if disagreement with the data

occurs, one must decide whether this is due to an incorrect equation of state or to a failure of the hydrodynamical approximation. The ability of these models to predict the kaon spectra could help distinguish these two cases. Unfortunately, at the moment, these models do not incorporate particle production. Perhaps the presentation of the data of this experiment will be a stimulant for the theorists to try to do so.

CHAPTER 2

EXPERIMENTAL METHODS

This experiment was performed at the Bevalac accelerator of the Lawrence Berkeley Laboratory. The Bevalac is able to accelerate heavy ion beams of mass up to Fe to energies between 400 MeV/amu and 2.1 GeV/amu. It was conceived in 1974 from a marriage of the then two independent machines, the Bevatron and the Hilac. The Hilac is a medium energy, 8.5 MeV/amu, highly intense heavy ion accelerator. In the Bevalac mode it is used as an injector of the Bevatron. The Bevatron is an historic machine. As a 6.2 GeV proton synchrotron it served at the frontiers of high energy physics from the mid '50's to the mid '60's. Now, in the Bevalac mode, it is used to accelerate the Hilac injected, heavy ion beams to energies up to 2.1 GeV/amu.

1. Beam

Three types of beam particles were used: neon at 2.1 GeV/amu, deuterons at 2.1 GeV/amu, and protons at 2.1 GeV. The beam intensity used depended upon the angle at which the spectrometer was set. With the spectrometer at 15° the intensity used was typically $\approx 3 \times 10^6$ particles per pulse while, with the spectrometer at 80°, it was typically $\approx 10^8$ particles per pulse. For a description of beam characteristics see Table I.

2. Targets

The targets used were C, NaF, KCl, Cu, and Pb. The thicknesses in gm/cm^2 were: C - 1.13, NaF - 1.20, KCl - 1.10, Cu - 0.92, Pb -

1.58. The thicknesses were chosen to be approximately 1 gm/cm^2 in order to provide a sufficient interaction rate while keeping the problem of multiple scattering within the target small.

3. Intensity Monitoring

In order to monitor the beam intensity we positioned an ionization chamber in the beam 1.5m upstream of our target. This chamber was in the beam during all phases of data taking. It consisted of 10 gaps filled with a gas mixture of 80% Ar and 20% CO_2 at 1.05 atmospheres of pressure. Before each period of data taking the chamber was calibrated by placing scintillation counters in the beam. For details of this calibration see Appendix A.

4. Particle Detection

Our detection apparatus consisted of two parts: a magnetic spectrometer and a set of scintillation counter telescopes.

4.1. Magnetic Spectrometer

The spectrometer is sketched in Fig. 5 with a vertical view shown in Fig. 6. The geometrical parameters of the various elements of the spectrometer are summarized in Table II. It consisted of the following elements.

4.1.1. Scintillation Counters

These consisted of counter G1, the five counters G2(A,B,C,D,E), and the three counters G3(U,C,D). All together they served five functions. First, counter G1 defined the solid angle acceptance of the spectrometer for particles emitted from the center of the target. Second, the logic

G1 · (G2A+G2B+G2C+G2D+G2E) · (G3U+G3C+G3D) defined the basic event trigger. This is what we call the inclusive trigger. Third, the velocity of the particle traversing the spectrometer was determined by measuring the time of flight between counters G1 and G3. The path length was 210 cm. and the FWHM of the resolution was 500ps. Fourth, the pulse heights in counters G1 and G3 were recorded in order to aid in particle identification and to determine if these counters suffered multiple hits. Finally, the five elements of G2 together with MWPC P5 helped to determine a "MATRIX" condition. The details of this will be discussed later.

4.1.2. Bending Magnet

This was a standard Bevatron C magnet with a gap spacing of 6" and pole tip dimensions of 13" x 24". As the charged particles traversed the magnetic field they were horizontally bent in accordance with the formula:

$$pc = zerB$$

where p is the momentum and ze is the charge of the particle. B is the field strength, and r is the radius of curvature. A measurement of r, therefore, determins the particle's rigidity, p/z. The radius was determined by measuring the angle into and out of the magnetic field. The relationship is:

$$L = r(\sin\theta_i + \sin\theta_o)$$

where L is the effective length of the magnet and θ_i and θ_o are, respectively, the angles into and out of the magnet. The magnetic field was mapped and was found to be uniform enough so that it could be

approximated by a constant field, 6.5kG, over a volume of 70.4cm x 33.0cm x 15.2cm. The error in the momentum arises from two sources. First, the finite wire spacing of the chambers led to some uncertainty in the angles. Second, multiple scattering of the particle, particularly while traversing G2, caused the outgoing angle to differ from its ideal value. Table III shows the momentum resolution as a function of the momentum as determined by a Monte Carlo simulation. The resolution is typically ± 10%.

4.1.3. Wire Chambers

These provided for the tracking of the particle through the spectrometer and, thereby, determined the ingoing and outgoing angles mentioned above. The ingoing angle was determined by P1X and P2X and the outgoing angle by P3X and P5.

A typical plot of TOF $\propto$ (velocity of the particle)$^{-1}$ vs. bending angle $\propto$ (charge/momentum) is shown in Fig. 7. It can be seen that for momentum up to 1 GeV/c the separation between protons and pions is very clean. However, in the region where we expect to see kaons we find no easily discernible events. The reason for this is that the yield of kaons is $\approx$ 1000 times smaller than that of protons and pions. Thus, in order to acquire satisfactory statistics on the kaonic events we would simultaneously acquire an exceedingly large quantity of events with protons and pions. More importantly, since the number of events which our data acquisition could handle was limited to $\approx$ 300 events/pulse, the amount of beam time required to accumulate these events would be exceedingly large. We, therefore, employed triggers which required more stringent criteria for determining acceptable events. In a hardware

sense, we incorporated a lucite Cerenkov counter and an array of lead glass blocks.

4.1.4. Lucite Cerenkov Counter

We wished to detect kaons in the momentum range of 350 MeV/c to 750 MeV/c. This corresponds to a range of beta, $0.58<\beta<0.84$. On the other hand, we wanted to reject pions with momentum as low as 300 MeV/c which corresponds to a beta of 0.90. We therefore needed a Cerenkov counter which responded when beta was between 0.84 and 0.90. For a threshold counter this would have required a material with an index of refraction between 1.12 and 1.19. There is no readily available material with this property. We chose, *therefore, to use lucite* which has a threshold beta of *0.67 and to use the principle* of total internal reflection.

Consider a particle *which is normally incident upon the counter.* The Cerenkov light is *emitted at an angle,* $\theta_c=\cos^{-1}\left[\frac{1}{\beta n}\right]$. On the *other hand, the angle for critical reflection* is given by $\theta_{cr}=\sin^{-1}\left[\frac{1}{n}\right]$. *Thus, if* $\theta_c<\theta_{cr}$, the light will pass through the face of the counter and be absorbed by opaque paper. Only if $\theta_c\geq\theta_{cr}$ will the light be totally internally reflected and reach the phototubes at the end. Thus the *effective threshold beta,* β_{th}, is *given by:*

$$\cos^{-1}\left[\frac{1}{\beta_{th} n}\right]\geq\sin^{-1}\left[\frac{1}{n}\right]$$

Which implies:

$$\beta_{th}\geq\left[n\cos\left[\sin^{-1}\left[\frac{1}{n}\right]\right]\right]^{-1}\geq.91$$

If the particle is not normally incident but enters at an angle θ_i, then

the threshold beta is lower. Here $\theta_c+\theta_i \geq \theta_{cr}$ for total internal reflection. Thus, because low momentum pions will be strongly bent in the magnetic field they will enter at a large angle and will, therefore, be easily rejected. A difficulty arises in that we wish to accept K's with beta up to 0.84. From the above, we see that this requires that $\theta_i < 5.2°$. For a particle emitted from the center of the target the entrance angle, θ_i, ranged from 9.1° to 16.0°. For a particle with a momentum of 750 MeV/c the corresponding outgoing angle, θ_o, ranged from 1.4° to -5.3°. As a result, in order to minimize the number of kaons rejected, the lucite counter was placed at an angle of -2.5° with respect to the axis of the spectrometer. This counter then allowed us to reject approximately 99% of the pions and except ≈ 80% of the kaons.

4.1.5. Lead-Glass Blocks

The array of lead glass blocks was used to detect the kaon decay products. Kaons with a momentum up to 750 MeV/c stopped in the array of blocks which was 162 gm/cm^2 long. The kaon has a lifetime of 12.4 ns. and decays 65.5% of the time to $\mu\nu$ with p_μ=236 MeV/c and 30.8% of the time to states containing π^0. Both of these types of decays created pulses in the lead glass. The μ's produced Cerenkov light directly while the π's decayed to two γ's which in turn produced showers of electrons and positrons which produced Cerenkov light.

These elements filtered out many of the unwanted particles. However, because the phototubes had slow rise times, it was not possible to use timing information to accept only signals from delayed decays. Therefore, high momentum protons which produced direct Cerenkov light in the Pb-glass blocks were accepted. In order to get

rid of these protons two additional trigger elements were adopted.

4.1.6. MATRIX

For a given entrance angle to the spectrometer, low momentum particles, being bent more than high momentum ones, hit MWPC P5 at a position closer to the beam axis. Counter G2 and chamber P5 were divided into 5 and 16 sections respectively. This division of G2 allowed a rough determination of the particle's entrance angle. For each of these five ranges of entrance angle there is a maximum distance from the x-axis at which a particle with momentum less than 750 MeV/c hits P5. We used a "MATRIX" to accept only events in which the particle hit closer to the beam axis than this maximum. This consisted of a 5 x 16 matrix of electronic gates. The inputs were the five G2 outputs and the 16 P5 outputs. Only events which had a G2-P5 combination which corresponded to a particle with momentum less than 750 MeV/c were accepted.

This eliminated some of the high momentum protons, but an unacceptable number were still getting through. The reason for this was two-fold. First, because each G2 segment accepted a large range of entrance angles, the position at P5 for particles of a definite momentum was quite dispersed. Therefore, if we set the "MATRIX" to accept with high efficiency particles with momentum less than 750 MeV/c, we would also accept quite a few particles with momentum greater than this since, even for 1 GeV/c, the minimum distance from the beam axis could be less than the maximum for 750 MeV/c particles. Second, if there were two particles in the spectrometer, we wished to accept the event if either one was in the acceptable momentum range. However, there

would then be a total of four possible G2-P5 combinations, and one of these would be apt to satisfy the criteria.

4.1.7. MBD

Finally, then, we employed an on-line, software cut based on an MBD (microprogrammable branch driver). The MBD was able to read the TOF and P3X and P5 wire chamber information before the event had actually been recorded. Based on this, it could then decide whether the event would fall above or below the dashed line shown in Fig. 7. If it would fall below the line, then the event was accepted. The MBD could make this decision in $\approx$ 100 μs. The result of this cut is shown in Fig. 8. Here the kaons are very clearly seen.

There was one difficulty associated with this cut. During a certain set of runs the cut rejected too many events. We compared particle spectra acquired in "normal" runs to those acquired in runs with the larger rejection in cases where the run conditions (beam, target, and spectrometer angle) were the same for the two types of runs. It was found that, to within 10%, the spurious rejection was independent of the momentum or type of particle. The data taken under these conditions were corrected accordingly.

4.2. Scintillation Counter Telescopes

Sixteen tag counter telescopes, each of which consisted of three scintillation counters, were situated around the target. Their function was to measure the associated multiplicity when a particle was detected in the spectrometer. They were situated symmetrically in azimuthal angle except for a section on one side which was left open in order not to

shadow the spectrometer. The θ and φ angular ranges and the solid angle subtended are shown in Table IV for each telescope.

4.3. Trigger Logic and Electronics

For a detailed discussion see Appendix B. The important point to mention here is the nature of the various triggers that were used. Each run had six triggers:

1) Inclusive trigger: $G1 \cdot G2 \cdot G3 \equiv G$

2) Pion trigger: $G \cdot Lucite$

3) Kaon trigger with MBD cut.

$G \cdot (Pb\text{-}glass) \cdot (Lucite\text{-}veto) \cdot Matrix \cdot (MBD\ cut)$

4) Kaon trigger without MBD cut.

$(G \cdot (Lucite\text{-}veto) \cdot (Pb\text{-}glass) \cdot Matrix)$

The following triggers varied from run to run so that the efficiency of the various trigger elements could be determined.

5) Kaon trigger with MBD cut missing one of the following:

(Lucite-veto, Pb-glass, Matrix)

6) Kaon trigger without MBD cut missing the same element as in 5 above.

4.4. Data Analysis

The data analysis was accomplished off-line on a CDC 7600 computer. This analysis took place in three stages:

1) determination of efficiency corrections

2) track reconstruction

3) kaon decay corrections

4) determination of the invariant cross sections

4.4.1. Efficiency Corrections

As mentioned in the previous section, the primary trigger consisted of the following elements: spectrometer, lucite Cerenkov veto, lead glass, and MBD. Here we analyze the corrections necessary for each of these elements.

Spectrometer. The spectrometer had a certain geometrical acceptance as determined by the size and position of the G-counters, wire chambers, and magnet gap. This acceptance was calculated by a Monte Carlo program with the above parameters as input. It determined whether particles which were emitted from the target at various angles and momenta passed through all of the elements. The result of this calculation is shown in Fig. 9 for particles emitted from the center of the target. In addition, however, there is a dependence upon the source distribution within the target. Therefore, on a run-by-run basis the observed target distribution was determined by extrapolating the particle trajectories back to the target using the front wire chambers. The actual target distribution was then determined by dividing by the geometrical acceptance for each target position. This distribution was then input to the Monte Carlo program to determine the final acceptance.

Although they were not a part of the trigger, the wire chambers were needed in order to accomplish the off-line tracking. Therefore, if any chamber did not fire, the event was rejected off-line. There was a total of nine planes of wire chambers. The efficiency of each plane was determined by requiring that all of the other planes fired and then checking the percentage of time that the plane in question also fired. The firing of the other eight planes guaranteed that the particle passed

through the plane in question. The efficiency of each plane was between 0.97–1.00, and the overall efficiency was 0.80–0.85. This varied somewhat from run to run depending primarily upon the instantaneous rate so, therefore, this procedure was carried out for each run.

Lucite Cerenkov veto. As mentioned above, we made some runs in which, in addition to the primary trigger, we also had a trigger with all elements except the lucite veto. By checking whether kaons which satisfied the latter trigger also satisfied the former, we could determine the fraction of kaons being rejected by the lucite veto. The result is shown in Fig. 10.

In order to accumulate pions we also had a trigger in which the lucite counter was used in a positive rather than a negative mode. It was found that for the pions in the momentum range of interest the efficiency was 99%.

Pb-glass. Some runs had a trigger with only the Pb-glass missing. The efficiency for kaons thus determined is shown in Fig. 11. Here the geometrical acceptance of the Pb-glass is also included. The efficiency is generally between 80% and 90%.

MBD cut. The MBD cut was always set conservatively so that even a few of the protons would satisfy the cut. Thus, no significant number of kaons were rejected by this part of the trigger.

4.4.2. Track Reconstruction

In order to select real particle tracks from the wire chamber data we required five criteria:

1) particle must originate from within certain

horizontal limits at the target (P1X,P2X)

2) particle must originate from within certain vertical limits at the target (P1Y, P2Y)

3) horizontal trajectories as determined by (P3X, P5) and (P1X, P2X) must meet at the magnet center within certain limits

4) vertical trajectories as determined by (P3Y, P2Y) and (P2Y, P1Y) must have the same slope within limits

5) the 45° P3 coordinate (P3U) must agree within limits with that expected from the P3X and P3Y coordinates.

Using these criteria, we were able to reject enough spurious tracks so that clean particle separation could be made and so that the background was sufficiently small. However, application of each of these criteria led to some inefficiency. In addition, because of multiple scattering in the G2 counter, those criteria involving the rear chambers, P3, P4, and P5, had a $p\beta$ dependence. In order to determine these efficiencies the events were required to satisfy the four criteria other than the one being tested. For those criteria which had a $p\beta$ dependence the spectrum of protons in a range equal to that of the kaons was compared before and after application of the criteia. All of the studies were made on a run by run basis. Table V shows typical efficiencies for each of the criteria and Fig. 12 shows the combined $p\beta$ dependence.

Once the trajectory was determined, the bending angle and therefore the momentum was determined. Then, by examining the bending angle versus TOF, a clean identification of the kaons could be made.

4.4.3. Decay of Kaon in Flight

Kaons have a proper lifetime of 12.4 ns. Therefore, the number that decay before reaching G3, which is 249 cm from the target, is not insignificant. The procedure for making this correction, however, is very simple. The correction factor is given by:

$$exp\,(L/\beta\gamma ct)$$

where βc is the kaon velocity, γt is the Lorentz dilated lifetime, and L is the distance the kaon must travel in order to be detected. Table VI shows these corrections factors as a function of the kaon momentum. One possible complication is that the μ from the K-decay may make it through the system and mimic the kaon. This problem was studied, and it was found that the chance of this happening was less than 1%-2%.

4.4.4. *Invariant cross section*

The invariant cross sections were determined by the formula:

$$\frac{Ed\sigma}{p^2dp} = \frac{Energy}{(Momentum)^2} \times \frac{(\#\ K's\ detected\ per\ pulse)}{efficiency \times \rho \times L \times N \times \Omega}$$

Where ρ is the density of nucleons in the target, L is the length of the target, N is the number of beam particles per pulse, and Ω is the solid angle subtended by the spetrometer.

4.5. Sources of Error

Table VII summarizes the corrections made to the data and the associated errors. These are separated into those which have little or no momentum dependence and those which do depend upon momentum. The overall absolute error is ≈ 30 %. The relative errors for the cross sections at different values of momentum are less than 10%.

CHAPTER 3

RESULTS

In this chapter we present the experimental results. We cover the following features of the K^+ data: comparison with thermal and cascade models, comparison of the momentum spectra for pp, p-nucleus, and nucleus-nucleus collisions, A-dependence, estimate of the relative values of the cross section for K^+ production in pp, p-neutron, neutron-neutron collisions, a measurement of the total K^+ production cross section for Ne+NaF and its relation to the nucleon-nucleon cross section, and associated multiplicities.

1. Model Comparisons

We first compare the experimental data with the models (row-on-row, and thermal) described in chapter 1. Shown in Figs. 13 to 18 are the measured momentum spectra of K^+ for several projectile and target combinations. We begin with model comparisons to the Ne+NaF and p+NaF spectra.

1.1. Row-on-Row Models

The kaon momentum spectra from Ne+NaF collisions as calculated using the row-on-row model[26] are shown in Fig. 17. The calculations have been multiplied by a factor of two in order to bring them more into agreement with the data. In this model the constituent nucleons of the nuclei are assumed to have a momentum distribution of the form of a Fermi sphere with a sharp cut off. The calculated kaon yields are too low, but, more importantly, the slopes of the spectra are too steep.

and their fall off with laboratory angle is too great. The dashed curves are based on the same model, but now the K's are allowed to scatter off of the calculated proton distributions.[27] Again, the calculations have been multiplied by a factor of two. The average number of scatterings is estimated by considering the K^+N cross sections and the number of nucleons in the colliding system. For Ne+NaF this average number of scatterings is 0.68. The fall off with lab angle and the slopes of the spectra now agree well with the data although the slopes are still somewhat too steep. There is also an overall normalization difference of a factor of ≈ 2, but, since the $NN \rightarrow K^+X$ cross sections are not very well known at these energies, this difference may not be significant.

In Fig. 19 is shown a plot of the differential cross section vs. energy in the nucleon-nucleon center of mass. There is an exponential fall off with energy. In addition, the data at different laboratory angles tend to lie all on the same curve. This indicates that the cross section is a function of E_{CM} only and does not depend strongly on the angle in the nucleon-nucleon center of mass frame. Also shown in the figure are the calculations of the row-on-row model with kaon scattering. These show an exponential trend, but they are not isotropic. The calculated cross sections are smaller for angles closer to 90° in the nucleon-nucleon center-of-mass. Fig. 20 shows a similar plot in the nucleon-nucleon frame for p+NaF. Once again, we see an isotropic, exponential behavior. Also plotted are the row-on-row calculations. Since the number of nucleons in the system is half that in the Ne+NaF case, the average number of kaon scatterings is smaller. In addition, here, the K's are assumed to scatter off of the stationary target nucleons. Due to this last fact, the calculated cross sections are even

more anisotropic and more in disagreement with the data.

Thus, the row-on-row model has so far been unable to give a satisfactory explanation of the data. In order to reproduce the momentum spectra some amount of kaon scattering is required. This, however, leads to far more anisotropy than is observed in the data.

1.2. Thermal Models

The simple thermal models, which ignore the effects of angular momentum, predict isotropy in the center of mass for Ne+NaF collisions. Also, if the kaons are assumed to be in thermal equilibrium, then the kaon scattering is necessarily incorporated. Fig. 21 shows the calculation of one such model[30] which assumes that the N's, K's, π's, Δ's, Σ's, and Λ's are all in both thermal and chemical equilibrium. The calculated shapes agree well with the data, particularly at 35° and 55°. In addition, the exponential behavior observed in Fig. 19 is what a thermal model would predict. Nevertheless, there are various difficulties with this model.

First, the absolute values of the calculated cross sections are a factor of 20 too high. This is a result of the fact that this model assumes that the kaons are in chemical equilibrium. However, since the absorption cross section of the kaons is very small, there is probably not enough time during the collision for the kaons to come to chemical equilibrium.

Secondly, it seems that, the interpretation of the exponential slope in Fig. 19 in terms of a temperature is not valid. If we do make this interpretation, we obtain a kaon temperature of 122 MeV for Ne+NaF. If we, then, make a similar plot for Ne+Pb as in Fig. 22, we again obtain

an exponential but here the temperature is 160 MeV. However, the fireball should have the largest temperature for collisions in which the target and projectile masses are equal since, then, the energy per nucleon avalalable to the fireball in the fireball rest frame is largest.

Finally, as previously mentioned, the p+NaF data also show an isotropic, exponential behavior in the nucleon-nucleon center of mass. Here the slope corresponds to a temperature of 111 MeV. However, the simple fireball model which does not incorporate the complexities introduced by angular momentum considerations predicts isotropy in the fireball rest frame. For the case of p+NaF this is very close to the target rest frame. The model would therefore predict a large anisotropy in the nucleon-nucleon CM frame. Also, since thermalization requires a large number of collisions, the thermal assumption would not seem to be appropriate for p-nucleus collisons. Thus, since the exponential behavior is common to both p-nucleus and nucleus-nucleus collisions, it probably reflects some mechanism other than thermalization.

We conclude from the above that, although the kaon spectra show some characteristics of a thermal distribution, there is no compelling evidence that the K's are indeed thermalized. Thus, at this time, there is no model which satisfactorily reproduces all of the significant features of the data. It would, therefore, be very interesting to incorporate particle production into the hydrodynamic models so that a comparison with the data could be made.

2. Comparison of pp, pA, and AA Collisions

Fig. 22 shows plots of the differential cross section for Ne+Pb and p+NaF vs. E_{CM} as measured in this experiment. Also plotted are data

on $pp \rightarrow K^+X$ at a laboratory kinetic energy of 2.54 GeV from a different experiment.[17] We see that there is a large difference between the pp and the p-nucleus data. On the other hand, the p-nucleus and nucleus-nucleus spectra look qualitatively the same. The main difference is a slight change in slope. It, therefore, seems that, at least at this gross level of description, the transition from pp to p-nucleus may contain the most interesting physics.

Shown in Fig. 20 are plots of calculations[31] made by extrapolating the $pp \rightarrow K^+X$ data down from higher energies to 2.1 GeV. The lower curve is with no Fermi momentum while the other is obtained by giving one of the nucleons a Fermi distribution of the form of a sharp sphere with p_F=270 MeV/c. It can be seen that, the curve with Fermi motion is still off by a factor of ten at the larger center of mass energies. In the previous section we have seen the effects of allowing the K's to scatter off of the target nucleons. As we saw, this led to a large amount of anisotropy. Therefore, neither conventional Fermi motion nor kaon scattering can account for the anomalously large production of high momentum kaons.

Since the p-nucleus data is fundamental to understanding the nucleus-nucleus data, and since the physics here may be very interesting, much of the current effort should be expended toward explaining its features. Specifically, we should examine whether the disagreement of the row-on-row calculation with the p-nucleus data is due to bad assumptions in the calculation or whether there is something unexpected and interesting happening here.

One possible mechanism to consider is the production of kaons via the reaction $\pi N \rightarrow K^+ X$. The threshold center of mass energy for this reaction is 1.61 GeV. This implies that, for a pion incident upon a stationary nucleon, the pion momentum must be >900 MeV/c. The cross section is largest for pions with momenta between 1 and 2 GeV/c, and, here, it varies from 100 to 500 μb. From existing data we estimate the cross section for production of pions of this momentum to be ≈ 5 mb per NN collision. We therefore estimate the cross section for kaon production via this mechanism to be:

$$\sigma(NN \rightarrow \pi X, 1GeV/c \leq P_\pi \leq 2GeV/c) x \frac{\sigma(\pi N \rightarrow K^+ X)}{\sigma(\pi N \rightarrow X)} \approx 5mb \frac{0.5}{30} = 0.08mb.$$

The cross section for $NN \rightarrow K^+ X$ is ≈ 0.05 mb. Therefore, we find that production via pions may be significant. Note that in these estimates we have made a couple of assumptions. One leads to an overestimation and the other to an underestimation of the number of effective pions. First, we have ignored the fact that most pions probably come from Δ decay. Since the Δ has a finite lifetime, some will decay outside of the reaction volume, and the resulting pions will not be available for the production of kaons. On the other hand, we have neglected the effect of Fermi motion in the target nucleons. This will reduce the threshold pion momentum and, therefore, lead to more pions being effective.

Having determined that this may be an important production mechanism, we next examine whether the produced kaons are in the appropriate kinematical region to account for the data. Specifically, we are interested in kaons with large energy in the nucleon-nucleon center of mass.

As noted, the cross section is largest for pion momentum between 1 and 2 GeV/c. In fact, the cross section has a sharp peak at around 1.5 GeV/c. This corresponds to a center of mass energy, $\sqrt{s}$, equal to 1.93 GeV. For simplicity, we assume that it is a delta function here. Fig. 23 shows a rapidity-P_T plot indicating the kinematic region covered by this experiment. Curves are drawn indicating where the kaons would lie for three different cases. These are for a pion incident upon a nucleon where the nucleon has: no Fermi momentum, 270 MeV/c of Fermi momentum parallel to the incoming pion, and 270 MeV/c anti-parallel to the pion. In each case we select the pion momentum such that the center of mass energy is 1.93. We see that kaons are produced in the region of relatively large energy. This is where the simple NN production model greatly underpredicts the cross section.

3. A - Dependences

We next study the A-dependence of the kaon production. We integrate the kaon cross sections over the momentum range covered in this experiment, 350 MeV/c to 750 MeV/c, for each lab angle. The result is shown in Fig. 24 for Ne incident on various targets. If we assume that the cross section is proportional to some power of the target mass, A_T^{α}, then, as seen in Fig. 24, α increases from 0.90 at 15° to 1.28 at 80°. We plot the values of α vs. the energy of the kaon in the NN center of mass in Fig. 25. Also plotted are the values with the deuteron projectile. We see an increase of α with E_{CM} for both cases. However, the values of α are consistently higher in the case of the Ne projectile.

In Fig. 25 we also plot the values of α when a pion is detected. For small values of E_{CM}, α is approximately the same for both Ne and d. At larger values of E_{CM}, α is somewhat higher in the case of Ne. Here, however, the difference is less than in the case of kaon production. We conclude that the target mass dependence for kaon production with the Ne projectile is anomalously large when compared to that with the deuteron projectile. This effect can not be explained in terms of simple geometry. It must, somehow, be related to a difference between the d+A and the Ne+A systems. There are at least three important differences.

First, the relative increase in the size of the system from Ne+NaF to Ne+Pb is less than that between d+NaF and d+Pb. This means that changes in absorption and multiple scattering effects could be different in the two cases. Kaons, however, suffer less absorption and multiple scattering than protons and pions. Since the effect is the largest for kaons, we conclude that absorption and multiple scattering are not the cause.

A second possibility arises from the difference in Fermi momentum between deuterons and Ne. As the nucleons interact with one another, their relative velocity decreases due to elastic scattering and energy loss in inelastic collisions. Since the incident energy of 2.1 GeV/amu is only slightly above threshold for kaon production, this energy loss is important. It may be, therefore, that in a large target all of the NN collisions may not be effective in kaon production. Therefore, the extra energy that the Ne nucleons have compared to those of the deuteron may lead to a larger number of effective collisions in the Pb target.

We have made a rough calculation of this effect and find that the trend is in the right direction.

The last effect that we mention may be the most interesting. This is the possibility of collective effects. It is possible that the initial interactions between the Ne and Pb nucleons will set up some sort of condition such that kaon production in succeeding collisions is enhanced. For example, the initial interactions may set up a high density region in which several nucleons may interact coherently. Also, the two-step process mentioned in section 2, $NN \rightarrow \pi N$ followed by $\pi N \rightarrow K^{+} X$, may be an example of this.

4. *Relative Cross Sections for pp, pn, nn*

In Fig. 26 we show the projectile mass dependence, A_p^{α}, which is calculated by comparing the kaon yield with a proton projectile to that with a deuteron projectile. We see the interesting feature that at small angles the ratio of cross sections with a deuteron to those with a proton projectile is comparatively small. A_p^{α} with $\alpha \approx .35$. We believe that this is related to the relative values of the pp, pn, and nn K^{+}-production cross sections. Taking into account the probability of the various NN collisions and neglecting shielding effects, we expect the ratio of $\sigma(d+NaF \rightarrow K^{+} X)$ to $\sigma(p+NaF \rightarrow K^{+} X)$ to be:

$$\frac{10 + 21R_{pn} + 11R_{nn}}{10 + 11R_{pn}}$$

where

$$R_{pn} = \frac{\sigma(pn \rightarrow K^{+} X)}{\sigma(pp \rightarrow K^{+} X)} \quad \text{and} \quad R_{nn} = \frac{\sigma(nn \rightarrow K^{+} X)}{\sigma(pp \rightarrow K^{+} X)}.$$

Here we have assumed that $R_{pn} = R_{np}$. The possible reactions are:

$pp \rightarrow p\Lambda K^+$ $\quad$ $pn \rightarrow n\Lambda K^+$ $\quad$ $nn \rightarrow n\Sigma^- K^+$

$\rightarrow p\Sigma^0 K^+$ $\quad$ $\rightarrow n\Sigma^0 K^+$

$\rightarrow n\Sigma^+ K^+$ $\quad$ $\rightarrow p\Sigma^- K^+$

We follow the procedure of reference 26 to estimate the relative values of these cross sections.

The one-pion-exchange model is assumed. This gives the following relation for the cross section:

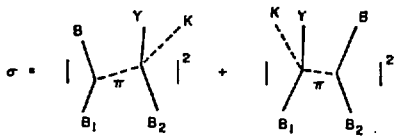

The interference term is ignored. We then find the relations shown in Table VIII. Here, G_Y^I is the square of the $\pi N \rightarrow YK$ coupling constant with an intermediate, isospin state of isospin = I. Existing data[32] show that:

$$\sigma(pp \rightarrow p\Lambda K^+) : \sigma(pp \rightarrow p\Sigma^0 K^+) : \sigma(pp \rightarrow p\Sigma^+ K^0) \approx 2.5 : 1 : 1$$

These relations imply:

$$G_\Lambda^{1/2} : G_\Sigma^{1/2} : G_\Sigma^{3/2} \approx 5 : 2 : 1.$$

Using thses values, we find that R_{pn}=1.5±0.4 and R_{nn}=0.17±.09. Since the reaction, $nn \rightarrow K^+\Lambda N$, cannot occur, it is reasonable that R_{nn} is quite small. Finally we predict:

$$\frac{\sigma(d + NaF \rightarrow K^+X)}{\sigma(p + NaF \rightarrow K^+X)} = 1.6 \pm 0.1.$$

At 15° we find this ratio to be = 1.3±0.2.

At 60° the ratio of $\sigma(p+A\rightarrow K^+X)$ to $\sigma(d+A\rightarrow K^+X)$ is larger with α=0.93 for the Pb target and α=0.81 for NaF. This is probably because this region is partially beyond the kinematical limit for kaon production if only one of the nucleons has conventional Fermi momentum. Therefore, the Fermi momentum of the deuteron is probably important in this region.

5. Total Cross Sections

We wish to measure the total K^+ production cross section in the nucleus-nucleus collisions and compare with the cross section in pp collisions. Unfortunately, this experiment covered a very narrow kinematical region. Therefore, it is unfeasible to attempt to determine the total cross section by simply extrapolating the fitted curves of the spectra without using any assumptions. The uncertainties would be too large. We can, however, use the observation that the cross sections are approximately isotropic in angle and exponential with energy in the NN centc of mass. We obtain, then, a measurement of the the total K^+ cross section by integrating curves such as those in Figs. 13-18. We extrapolate the exponential and then integrate over angle by assuming isotropy. The values so obtained are shown in Table IX. Because this experiment covered only a small part of the total kinematic region available to the kaons, for the cases of unequal target and projectile masses, the validity of this technique is somewhat questionable. However, for the case of Ne+NaF the assumption of isotropy is more realistic, and the obtained values are much more reliable. We concentrate, therefore, on this case.

The value of the total cross section for K^+ production that we obtain for Ne+NaF is 23±8 mb. Fig. 1 shows the pp data for the reaction $pp \rightarrow p\Lambda K^+$ and $pp \rightarrow p\Sigma^0 K^+$. When p_{beam} = 2.89 GeV/c, we estimate that

$$\sigma(pp \rightarrow p\Lambda K^+) = 20\pm10 \ \mu b \text{ and } \sigma(pp \rightarrow p\Sigma^0 K^+) = 5\pm5 \ \mu b.$$

The isospin analysis of the previous section with $G_\Lambda : G_\Sigma^{1/2} : G_\Sigma^{3/2}$ = 2.5 : 1 : 1 implies that

$$\sigma(pp \rightarrow n\Sigma^+ K^+) = 15\pm15 \ \mu b$$

giving

$$\sigma(pp \rightarrow K^+ X) = 40\pm19 \ \mu b.$$

Since both Ne and NaF have approximately equal numbers of neutrons and protons, we wish to compare with the isospin averaged NN cross section. Using the values of R_{pn} and R_{nn} found in the previous section, this cross section is 1.04 times the pp cross section. We find, then, that:

$$\frac{\sigma(Ne + NaF \rightarrow K^+ X)}{\sigma(N + N \rightarrow K^+ X)} = 575\pm338.$$

Therefore, if the cross section can be parametrized by $(A_P A_T)^\alpha$ then α=1.05±0.1. It is equal to one within the errors. A value of α greater than one would imply some form of collective effect.

6. Multiplicity

We next turn to a study of the multiplicity of charged particles in the events in which a kaon, pion or proton is detected in the spectrometer. It should be recalled that we had 16 tag counter telescopes surrounding the target. These telescopes were sensitive to

charged particles. However, in order to be detected by these telescopes, the particle must have passed through approximately 5.5 g/cm^2 of material. Thus, protons with energy less than 100 MeV and pions with energy less than 25 MeV were not detected. The telescopes consisted of two sets. A set of seven counters covered polar angles from 24.1° to 36.0° in the laboratory frame while a set of nine counters covered polar angles from 36.0° to 58°.

The method described in reference 33 relates the measured experimental quantities, $P_{NP} = \frac{R_P^N}{R_S}$, to the moments of the actual multiplicity distribution. Here, R_P^N is the rate of coincidence between the spectrometer and p of the N tag counters, and R_S is the singles rate of the spectrometer. The quantities actually determined are:

$$\langle M-1\rangle\Omega,\ \langle (M-1)(M-2)\rangle\Omega^2,\ \langle (M-1)(M-2)(M-3)\rangle\Omega^3,\ etc.$$

Where M is the average multiplicity. The quantity Ω is the effective solid angle of each counter. It is defined by:

$$\Omega = 4\pi \times \frac{\int_{\varphi_{min}}^{\varphi_{max}} \int_{\cos\theta_{min}}^{\cos\theta_{max}} f(\theta) d\cos\theta d\varphi}{\int_0^{2\pi} \int_{-1}^{1} f(\theta) d\cos\theta d\varphi}$$

where $f(\theta)$ is the angular distribution of particles and the angles, θ_{min}, θ_{max}, φ_{min}, and φ_{max}, are determined by the size and position of the counters. The largest uncertainty in this analysis is due to the difficulty in estimating the function, $f(\theta)$.

If we assume that the angular distribution of all particles is the same as the angular distribution of the inclusive particles measured in a

previous experiment,[34] we find that $f(\theta)$ can be approximated by $Ae^{-\theta/\gamma}$ where $\gamma \approx 29°$, and θ is the lab angle. The sixteen counters were divided into a set of seven and a set of nine. We expect the distribution to be forwardly and backwardly peaked in the nucleon-nucleon center of mass system. Thus, there may be some deviation from the exponential behavior in the vicinity of 180° in the lab. However, the number of particles here is quite small compared to the total number and will not seriously effect the results.

Because of a difference in size and angular placement, the effective solid angles of the counters in the two sets are different. We measure $\langle M-1\rangle\Omega'$ for the set of seven counters and $\langle M-1\rangle\Omega''$ for the set of nine. We find that $\Omega'/\Omega'' = 1.23$. We know the difference in geometrical solid angle for the two sets of counters and can factor it out. To account for the remaining difference, we find that a value of $\gamma \approx 29°$ is required. This gives us confidence that the assumed distribution is not too unrealistic. On the other hand, because there are many fewer events with kaons, the statistics for these events are worse. From run to run the Ω'/Ω'' ratio varies by a significant amount. We have assumed the angular distribution for kaons to be the same as for protons and pions. However, it can be significantly different and still agree, within errors, with the observed Ω'/Ω'' ratio. The multiplicity could then differ by approximately 10% form the tabulated values.

Table X shows the values of the multiplicities obtained by this method. For the case of Ne+Pb we see that the multiplicity when a kaon is detected in the spectrometer is systematically slightly higher than when a pion is detected. In most models the multiplicity monotonically

increases with decreasing impact parameter. Here, impact parameter means the distance between the centers of the colliding nuclei at their point of closest approach. Interpreted in this light, Table X indicates that, as compared to protons, kaons tend to come from more central events while pions are biased toward more peripheral ones. Since pions have a relatively large absorption cross section, it may be that those produced in the central region tend to be absorbed before they get out, while those produced on the periphery, which traverse less of the nuclear matter, have a lower probability of being absorbed. For Ne+NaF we see that the multiplicities are, within errors, approximately all the same. This, however, may be consistent with the above since the difference between central and peripheral events is not as great for Ne+NaF as for Ne+Pb.

Unfortunately, it seems very difficult to draw any more substantial conclusions from the multiplicity data at this time. This is partially due to the fact that the difference in multiplicity for the various particles is not very large. For Ne+Pb the multiplicities differ by about 10%. Also, however, because of the uncertainty in the angular distributions, the data are ambiguous.

7. Conclusions

We may summarize the results of this chapter as follows.

1) A simple cascade model[26,27] incorporating conventional Fermi momentum and kaon scattering is able to reproduce the general trends of the data. However, it predicts too much anisotropy in the nucleon-nucleon center of mass system.

2) A thermal model[30] can be constructed which fits the shape of the observed spectra. The agreement is probably fortuitous, however, and the thermal model is rejected for the following reasons. The calculated yields of the kaons are too great by a factor of 20. The temperature of the kaons measured from the exponential slopes of the energy spectra is much higher than that of protons and pions. The thermal-like features of the exponential spectra are also observed in p-nucleus collisions. The p-nucleus data are not isotropic in the fireball rest frame which is contrary to the thermal model prediction.

3) One of the most interesting features of the data is the difference between the spectra in pp and p-nucleus collisions. For p-nucleus collisions the excess of kaons with a large momentum in the nucleon-nucleon center of mass is of particular interest. No model has yet been able to explain this difference satisfactorily. Kaon production via $\pi N \rightarrow K^+ X$ is one feature which has not been incorporated into the models and which may be important in explaining the data.

4) The A-dependence of the kaon yield has the interesting feature that the target mass dependence is greater for heavier projectiles. Also, the projectile mass dependence is greater for heavier targets. This is not what one expects from models based on simple geometry with independent NN collisions. It may, therefore, indicate some form of collective behavior.

5) The estimated, total cross section for K^+ production in Ne+NaF collisions be characterized by $(A_P A_T)^{\alpha}$ with $\alpha \approx 1.05 \pm 0.1$. The cascade model incorporating multiple scattering predicts $\alpha=1$. Within the errors,

the measured value agrees with this.

6) Measurement of the associated multiplicities. M_K, M_π, M_p in which a K, π, or proton is detected in the spectrometer show that for Ne+Pb $M_K \approx M_p+1 \approx M_\pi+2$ while for Ne+NaF $M_K \approx M_p \approx M_\pi$. This suggests that events in which a kaon is detected are biased more toward central collisions while those in which a pion is detected are biased more toward peripheral ones.

As mentioned in Chapter 1, one of the primary goals of the study of K^+ mesons in heavy ion collisions is to learn about the early stage of the reaction. This depends upon the fact that the K's have a long mean free path. However, before undertaking such an ambitious program, we must first develop a better understanding of the basic K^+ production mechanism and determine whether the assumption of a long mean free path is indeed valid. This experiment has given a start at answering these questions.

We have found that simple nucleon-nucleon collisions with conventional Fermi momentum distributions cannot explain the data. It seems that a two-step process of the type $NN \rightarrow \pi X$ followed by $\pi N \rightarrow K^+ Y$ is a possible alternative production mechanism. However, at this time we cannnot make a definitive statement on this but must wait for its incorporation into the cascade codes.

The near isotropy of the kaon spectra in the nucleon-nucleon center of mass indcates that, as expected, the kaons suffer only a small amount of scattering. Since, however, this experiment covered only a limited kinematical region, future work is needed to see if this isotropy exists over the entire region. If it does, then this will be very strong

evidence that the kaons, as hoped, can be used as messengers of the early stages.

Another question which deserves greater study is that of the A-dependence. As mentioned in 5) above, we have observed what may be an interesting effect. However, this is based on comparisons between neon and deuteron projectiles. Because of small Fermi momentum the deuteron is an unusual nucleus. It is not known now whether this is the cause of the observed effect. The uranium beam soon to be developed at the Bevalac may be particularly useful in this study.

Finally, we mention that since K^+ and Λ are closely related by the principle of associated production, the study of Λ production in relation to K^+ production is of some interest. Recently Λ's have been measured in a streamer chamber experiment.[35] Large number of Λ'S with momenta much larger than that expected from free nucleon-nucleon collisions were observed. Although the statistics on the Λ production are low, it would, nevertheless, be interesting to study whether the K^+ and Λ spectra are consistent.

We expect, then, that, particularly with the heavier beams soon to be available at the Bevalac, the measurement of strange particle production should be a very interesting endeavor. Hopefully, the present experiment will have played a useful role by helping to lay the groundwork.

Table I. BEAM PARAMETERS

Size at Target (FWHM)	7 mm V, 7 mm H
Spill	≈ 2 sec
Repetition Rate	≈ 6 sec
Transmittance (FWHM)	$\Delta x \Delta \theta_x$ = 0.8 inch· mrad.
	$\Delta y \Delta \theta_y$ = 1.5 inch· mrad

TABLE II. SPECTROMETER ELEMENTS

Element	Position		Dimension		
	x(cm)	z(cm)	x(cm)	y(cm)	z(cm)
C Magnet	26.67	165.4	33.0	15.2	61.0
G1	8.57	38.35	5.08	3.81	0.64
G2 (5 vertical)	17.5	73.81	12.7	7.62	0.32
G3 (3 horizontal)	14.0	249.0	55.9	26.7	0.95
Lucite Cerenkov	14.0	254.1	61.0	30.5	5.08
Pb-Glass	14.0	322.5	60.0	45.0	45.0

Wire Chamber	Position		# of Wires		Wire Spacing (mm)
	x(cm)	z(cm)	x	y	
P1	8.64	41.22	64	64	1
P2	14.81	69.16	64	64	2
P3U	19.6	167.4	192	--	2
P3XY	19.6	187.3	192	192	2
P4	16.74	213.4	256	--	2
P5	16.96	228.6	256	--	2

For a definition of x, y, and z axes see Fig. 6

Table III. MOMENTUM RESOLUTION

P(Mev/c)	Δp/p resolution due to multiple scattering	Δp/p resolution due to wire spacing
300	7.8%	2.5%
400	6.0%	3.8%
500	5.0%	4.8%
600	4.3%	6.0%
700	3.9%	7.1%
800	3.6%	8.3%

TABLE IV. TAG COUNTER PARAMETERS

Counter	θ_{min}	θ_{max}	φ_{min}	φ_{max}	Solid Angle (mstr)
1	24.1	36.0	33.1	56.9	3.43
2	24.1	36.0	78.1	101.9	3.43
3	24.1	36.0	123.1	146.9	3.43
4	24.1	36.0	168.1	191.9	3.43
5	24.1	36.0	213.1	236.9	3.43
6	24.1	36.0	258.1	281.9	3.43
7	24.1	36.0	303.1	326.9	3.43
8	42.4	57.6	50.1	69.9	5.57
9	42.4	57.6	110.1	129.9	5.57
10	42.4	57.6	140.1	159.9	5.57
11	42.4	57.6	170.1	189.9	5.57
12	42.4	57.6	200.1	219.9	5.57
13	42.4	57.6	230.1	249.9	5.57
14	42.4	57.6	260.1	279.9	5.57
15	42.4	57.6	290.1	300.9	5.57
16	42.4	57.6	320.1	330.9	5.57

TABLE V. TRACKING EFFICIENCIES

Criteria*	1	2	3	4	5	Total
Efficiency	0.91	0.97	0.96	0.93	0.98	0.77

* For definition of criteria see page 26 of text.

TABLE VI. CORRECTIONS FOR KAON DECAY IN FLIGHT

Momentum	Correction Factor*
350	0.38
400	0.43
450	0.47
500	0.51
550	0.54
600	0.57
650	0.60
700	0.62
750	0.64

* Correction factor defined by: $N_{true} = N_{detected}$/Correction Factor

TABLE VII. EFFICIENCY CORRECTIONS AND ERRORS

Type of Correction	Correction* to cross section	Error** in cross section
Absolute Beam Intensity	0%	5%
Dead Time	30%	1%
MWPC Efficiency	20%	10%
Track Reconstruction	25%	10%
$\frac{dE}{dx}$ scatter plot cut	10%	3%
Decay in Flight	30%	1%
Spectrometer Acceptance	0%	5%
Pb Glass Efficiency	15%	15%
Anti Lucite Efficiency	30%	15%
Total		30%

* Correction value is defined as the per cent of the events lost due to the specified item. ** Error is in percent of cross section, not in percent of correction.

Table VIII. RELATIVE VALUES OF VARIOUS K^+ PRODUCTION REACTIONS IN TERMS OF COUPLING CONSTANTS

$$pp \rightarrow p\Lambda K^+ \quad \propto \quad \frac{2}{9}G_\Lambda$$

$$pp \rightarrow p\Sigma^0 K^+ \quad \propto \quad \frac{2}{27}G_\Sigma^{1/2} + \frac{8}{27}G_\Sigma^{3/2}$$

$$pp \rightarrow n\Sigma^+ K^+ \quad \propto \quad \frac{4}{3}G_\Sigma^{3/2}$$

$$pn \rightarrow n\Lambda K^+ \quad \propto \quad \frac{5}{9}G_\Lambda$$

$$pn \rightarrow n\Sigma^0 K^+ \quad \propto \quad \frac{5}{27}G_\Sigma^{1/2} + \frac{8}{27}G_\Sigma^{3/2}$$

$$pn \rightarrow p\Sigma^- K^+ \quad \propto \quad \frac{10}{27}G_\Sigma^{1/2} + \frac{4}{27}G_\Sigma^{3/2}$$

$$nn \rightarrow n\Sigma^- K^+ \quad \propto \quad \frac{4}{27}G_\Sigma^{1/2} + \frac{4}{27}G_\Sigma^{3/2}$$

$$pp \rightarrow p\Sigma^+ K^0 \quad \propto \quad \frac{4}{27}G_\Sigma^{1/2} + \frac{4}{27}G_\Sigma^{3/2}$$

Table IX. VALUES OF THE TOTAL CROSS SECTION FOR K^+ PRODUCTION

Reaction	σ_{TOT}
p + NaF	1.8 ± 0.6 mb
p + Pb	11 ± 4 mb
d + NaF	2.4 ± 0.8 mb
d + Pb	14 ± 5 mb
Ne + Naf	23 ± 8 mb
Ne + Pb	250 ± 90 mb

Table X. ASSOCIATED MULTIPLICITIES

NE + NaF

θ_{LAB}	M_p	M_π	M_K
35°	6.0 ± 0.5	6.2 ± 0.5	6.1 ± 0.5
55°	6.2 ± 0.5	7.2 ± 0.6	6.8 ± 0.6
80°	6.1 ± 0.5	7.1 ± 0.6	7.4 ± 0.6

Ne + Pb

θ_{LAB}	M_p	M_π	M_K
15°	18.5 ± 1.5	13.3 ± 1.1	18.5 ± 1.5
35°	20.1 ± 1.6	17.9 ± 1.4	22.4 ± 1.8
55°	22.1 ± 1.8	19.8 ± 1.6	23.1 ± 1.9
80°	21.1 ± 1.7	19.6 ± 1.6	22.6 ± 1.8
average	20.5 ± 1.0	17.6 ± 0.9	22.8 ± 1.1

REFERENCES

1. A. E. Glassgold, W. Heckrotte, and K. M. Watson, Ann. Phys. 6, 1 (1959).
2. G. F. Chapline, M. H. Johnson, E. Teller and M. S. Weiss, Phys. Rev. D8, 4302, (1973).
3. M. I. Sobel, P. J. Siemens, J. P. Bondorf and H. A. Bethe, Nucl. Phys. A251, 502 (1975).
4. G. F. Chapline, Proc. of the 2nd High Energy Heavy Ion Summer Study, Berkeley, Ca. 1974.
5. U. Heinz, H. Stöcker and W. Greiner, Proc of the Symposium on Reletivistic Heavy Ion Research, GSI Darmstadt, 1978.
6. M. Gyulassy, Lecture notes, INS Kikuchi summer School on Nuclear Physics at High Energies, INS, Tokyo, 1980
   The hydrodynamical assumption is that: $T_{rel} \ll T_{coll}$ where T_{rel} = relaxation time between successive NN collisions = (NN mean free path / velocity of the projectile) and T_{coll} = total collision time = (size of system / velocity of the projectile).
7. K. K. Gudina and V. D. Toneev, Dubna Report E2-12644, (1979).
8. J. Nix, Proc. of the Symposium on Reletivistic Heavy Ion Research, GSI Darmstadt, 1978.
9. A. B. Migdal, Rev. Mod. Phys. 50, 107, (1978).
10. W. Weise, and G. E. Brown, Phys. Reports 27C, 1, (1976).
11. J. M. Irvine, Rep. Prog. Phys. 38, 1385, (1975).
12. G. F. Chapline and M. Nauenberg, Phys. Rev. D 16, 450, (1977).
13. G. Baym and S. Chin, Phys Lett. 62B, 241, (1976).
14. D. N. Schramn, M. Crawford and K. A. Olive, Proc. of the Workshop

on Ultra-relativistic Nuclear Collisions. Berkeley, Ca. 1979.

15. Particle Data Group, Rev. Mod. Phys. 48, No. 2, Part II (1976)

16. π^+p, π^+n and π^+d Interaction - A Compilation, Particle Data Group, D. M. Chew, V. P. Henri, T. A. Lasinski, T. G. Trippe, F. Uchiyama, and F. C. Winkelmann, LBL-53, 1973

17. W. J. Hogan, P. A. Piroue and A. J. S. Smith, Phys. Rev. 166, 1472, (1968).

18. G. D. Westfall., J. Gosset, P. J. Johansen, A. M. Poskanzer, W. G. Meyer, H. H. Gutbrod, A. Sandoval, R. Stock, Phys. Rev. Lett. 37, 1202, (1976).

19. J. Gosset, J. I. Kapusta, G. D. Westfall, Phys. Rev. C 18, 844, (1978).

20. J. I. Kapusta, Phys. Rev C 16, 1493, (1977).

21. S. Nagamiya, Proc of the 4th High Energy Heavy Ion Summer Study, Berkeley, Ca., 1978.

22. R. K. Smith and M. Danos, Proc. of the Topical Conf. on Heavy Ion Collisions, Fall Creek Falls, Tenn., 1977.

23. Y. Yariv, and Z. Fraenkel, Phys. Rev. C 20, 2227, (1979).

24. J. Cugnon, T. Mizutani, J. Vandermeulen, Nucl. Phys. A 352, 505 (1981).

25. J. Hufner and J. Knoll, Nucl. Phys. A 270, 460, (1977).

26. J. Randrup and C. M. Ko, Nucl. Phys. A 343, 519, (1980).

27. J. Randrup, Phys. Lett. 76B, 547, (1978).

28. A. A. Amsden, G. F. Bertsch, F. H. Harlow, J. R. Nix, Phys. Rev. Lett. 35, 905, (1975).

29. A. A. Amsden, A. S. Goldhaber, F. H. Harlow, J. R. Nix, Phys. Rev. C 15, 2509, (1977).

30. F. Asai, H. Sato and M. Sano, Phys. Lett. 98B, 19, (1981).

31. J. Randrup, *unpublished*

32. *NN and ND Interactions* - A Compilation, Particle Data Group, O. Benary, L. R. Price, and G. Alexander, UCRL-20000NN (1970).

33. G. B. Hagemann, R. Broda, B. Herskind, M. Ishihara and S. Ogaza, Nucl. Phys. A245, 166, (1975)

34. S. Nagamiya, M. C. Lemaire, E. Moeller, S. Schnetzer, G. Shapiro, H. Steiner and I. Tanihata, LBL preprint 12123, (1981).

35. J. W. Harris, A. Sandoval, R. Stock, H. Stroebele, R. E. Renfordt, J. V. Geaga, H. G. Pugh, L. S. Schroeder, K. L Wolf, and A. Decal, Lawrence Berkeley Laboratory Report LBL-12334 (1981); to be published.

FIGURE CAPTIONS

Fig. 1 $\sigma(pp \to p\Lambda K^+)$ and $\sigma(pp \to p\Sigma^0 K^+)$ as a function of laboratory momentum.

Fig. 2 $\frac{d^2\sigma}{dpd\Omega}$ vs. P_{CM} for $pp \to K^+X$ with T_p=2.54 GeV.

Fig. 3 $\frac{d^3\sigma}{dp^3}$ vs. T_{CM} for Ne+NaF$\to$p+X and Ne+NaF$\to\pi^+X$ at θ_{CM}=90°.

Fig. 4 Comparison of the row-on-row calculation with data for 2.1 GeV/amu Ne+NaF and Ne+Pb $\to$p+X.

Fig. 5 Sketch of the spectrometer

Fig. 6 Vertical view of the spectrometer.

Fig. 7 Scatter plot of TOF vs. bending angle for events satisfying the inclusive trigger. Also shown is dashed line indicating the location of the MBD cut.

Fig. 8 Scatter Plot of TOF vs. bending angle for the full kaon trigger.

Fig. 9 Acceptance of the spectrometer as a function of momentum.

Fig. 10 Percentage of kaons rejected by the lucite counter veto as a function of kaon momentum.

Fig. 11 Pb-glass efficiency as a function of the kaon momentum.

Fig. 12 Efficiency of those off-line track reconstruction cuts which depend upon $p\beta$ (multiple scattering) as a function of momentum.

Fig. 13 Invariant cross section for d+NaF$\to K^+X$ vs. K^+ momentum for lab angles of 15°, 35°, and 60°.

Fig. 14 Invariant cross section for d+Pb$\to K^+X$ vs. K^+ momentum for lab angles of 15°, 35°, and 60°.

Fig. 15 Invariant cross section for p+NaF$\to K^+X$ vs. K^+ momentum for lab angles of 15°, 35°, 60°, and 85°.

Fig. 16 Invariant cross section for $p+Pb \rightarrow K^{+}X$ vs. K^{+} momentum for lab angles of 15°, 35°, 60°, and 80°.

Fig. 17 Invariant cross section for $Ne+NaF \rightarrow K^{+}X$ vs. K^{+} momentum for lab angles of 15°, 35°, 55°, and 80°. Also shown are calculations of the row-on-row model with and without kaon rescattering for lab angles of 35°, 55°, and 80°. The calculations have been multiplied by 2.

Fig. 18 Invariant cross section for $Ne+Pb \rightarrow K^{+}X$ vs. K^{+} momentum for lab angles of 15°, 35°, 55°, and 80°. Also shown are calculations of the row-on-row model with kaon rescattering for lab angles of 35°, 55°, and 80°. The calculations have been multiplied by 2.

Fig. 19 Triple differential cross section vs. E_{CM} in the nucleon-nucleon center of mass for $Ne+NaF \rightarrow K^{+}X$. Also shown are the calculations of the row-on-row model incorporating scattering of the kaons. Data are at lab angles of 15°, 35°, 55°, and 80°. Calculations are for lab angles of 35°, 55°, and 80°.

Fig. 20 Triple differential cross section vs. E_{CM} in the nucleon-nucleon center of mass for $p+NaF \rightarrow K^{+}X$. Also shown are the calculations of the row-on-row model incorporating kaon scattering and calculations for NN collisions with and without Fermi momentum. Data shown are for lab angles of 15°, 35°, 60°, and 80°. Row on-row calculations are for lab angles of 15°, 35°, 45°, 60°, and 80°. The NN calculations have been multiplied by a factor of ten in order to place them on the same scale.

Fig. 21 Comparison of the thermal model to the data for Ne+NaF→K^+X. The calculations have been divided by a factor of 20.

Fig. 22 Triple differential cross section for Ne+Pb→K^+X, p+NaF→K^+X, and p+p→K^+X vs. E_{CM} in the nucleon-nucleon center of mass. The Ne+Pb data has been divided by a factor of 10.

Fig. 23 Rapidity vs. P_T scatter plot showing the kinematical region covered by this experiment and the region populated by kaons produced via the reaction $\pi N \rightarrow K^+X$. Dashed curve shows the kinematical limit with a maximum Fermi momentum of 270 MeV/c.

Fig. 24 Kaon yield as a function of A_T for Ne+A_T→K^+X at lab angles of 15°, 25°, 35°, 45°, 55°, and 80°.

Fig. 25 α as a function of center of mass energy where α is defined by $\frac{d\sigma}{dp} \propto A_T^{\alpha}$ for kaon and pion yields.

Fig. 26 α as a function of lab angle for NaF and Pb targets where α is defined by (kaon yield)$\propto A_P^{\alpha}$.

Fig. 27 Ion chamber voltage vs. T·B coincidences.

Fig. 28 Ion chamber voltage vs. $\sum$ tag counters.

Fig. 29 Measured charge on the ion chamber per beam particle vs. charge calculated from the physical parameters of the chamber.

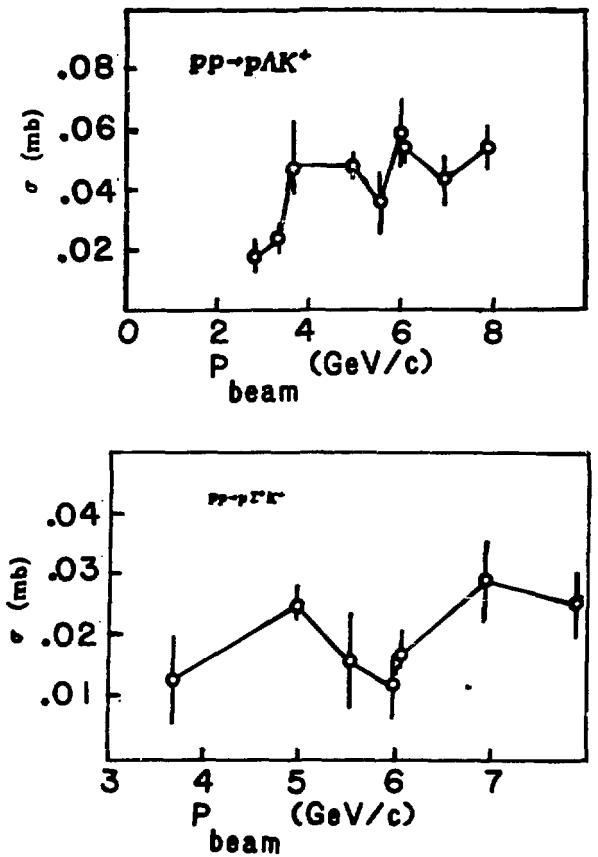
pp→pΛK⁺
.08
.06
.04
.02
σ (mb)
0
2
4
6
8
P beam (GeV/c)
.04
.03
.02
.01
σ (mb)
3
4
5
6
7
P beam (GeV/c)

Figure 1

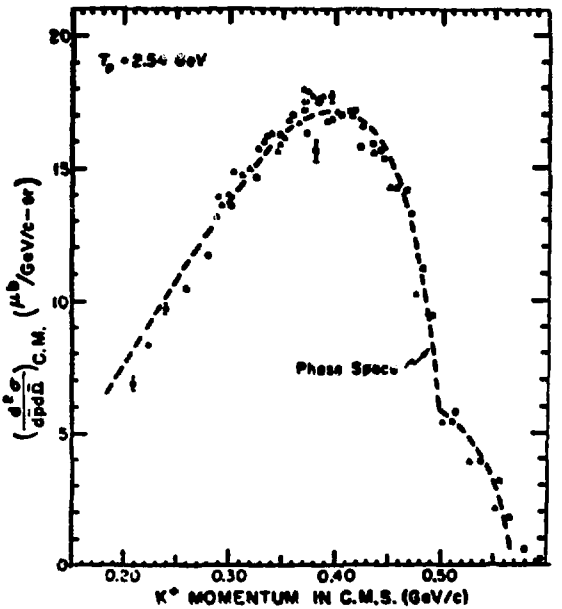
T_p = 2.54 GeV
Phase Space
$\left(\frac{d^2\sigma}{dpd\Omega}\right)_{C.M.}$ (μb/GeV/c-sr)
K* MOMENTUM IN C.M.S. (GeV/c)
0
5
10
15
20
0.20
0.30
0.40
0.50

Figure 2

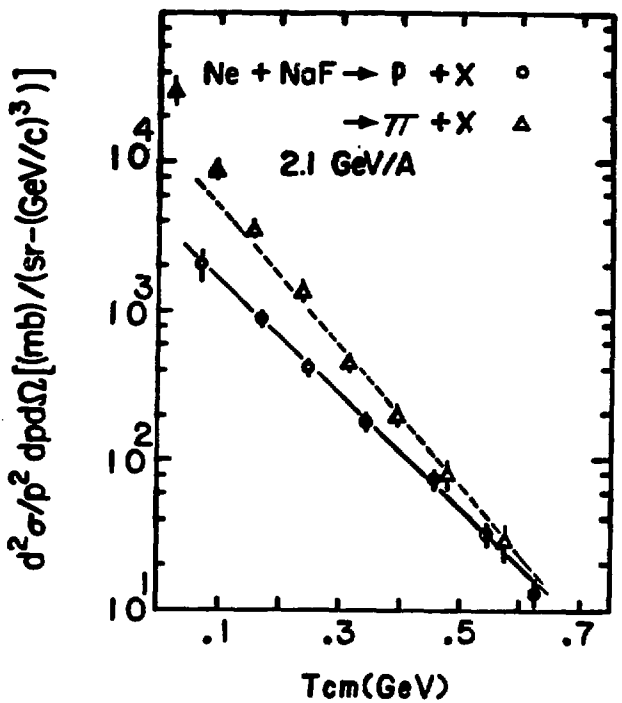
Ne + NaF → p +X
→ π +X
2.1 GeV/A
$d^2\sigma/p^2\,dpd\Omega[(mb)/(sr-(GeV/c)^3)]$
10^4
10^3
10^2
10
.1
.3
.5
.7
Tcm(GeV)

Figure 3

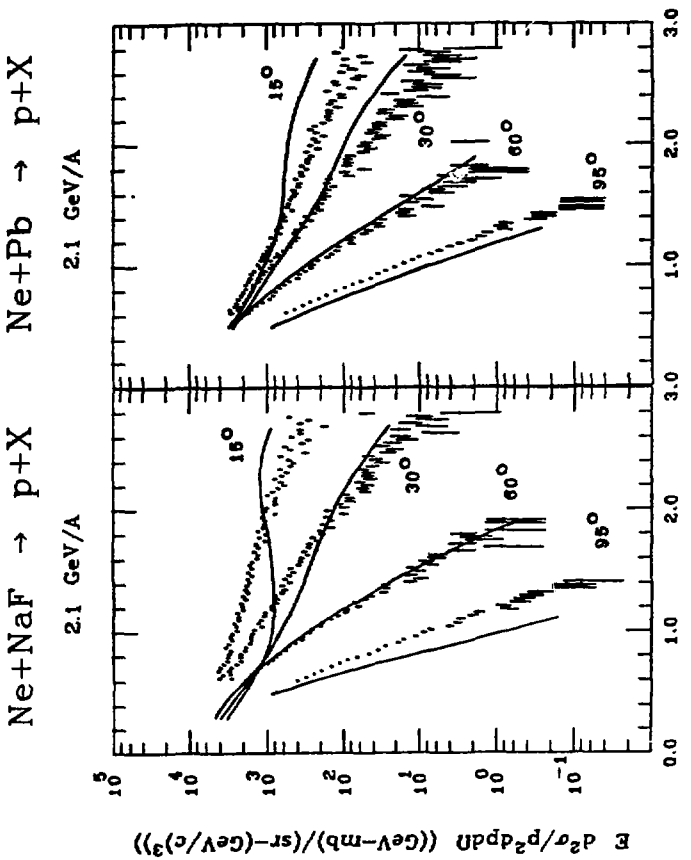
Ne+NaF → p+X
2.1 GeV/A
Ne+Pb → p+X
2.1 GeV/A
15°
30°
60°
95°
E d²σ/p²dpdΩ ((GeV−mb)/(sr−(GeV/c)³))
Momentum (GeV/c)
Momentum (GeV/c)

Figure 4

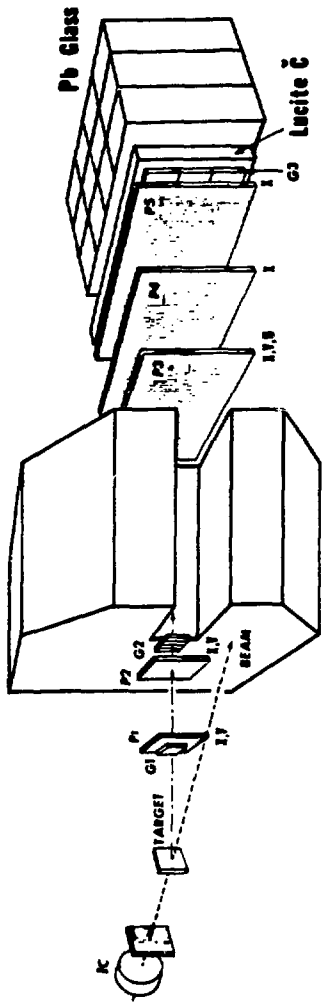

Figure 5

SPECTROMETER (TOP VIEW)

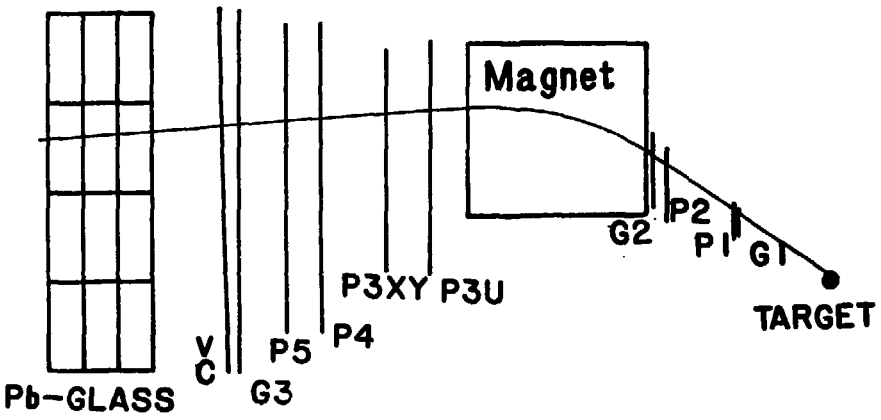

vertical scale
(2/5)xhorizontal scale

Figure 6

INCLUSIVE TRIGGER
deuteron
proton
(kaon)
pion
TOF ∝ 1/v
BENDING ANGLE ∝ 1/p

Figure 7

Figure 8

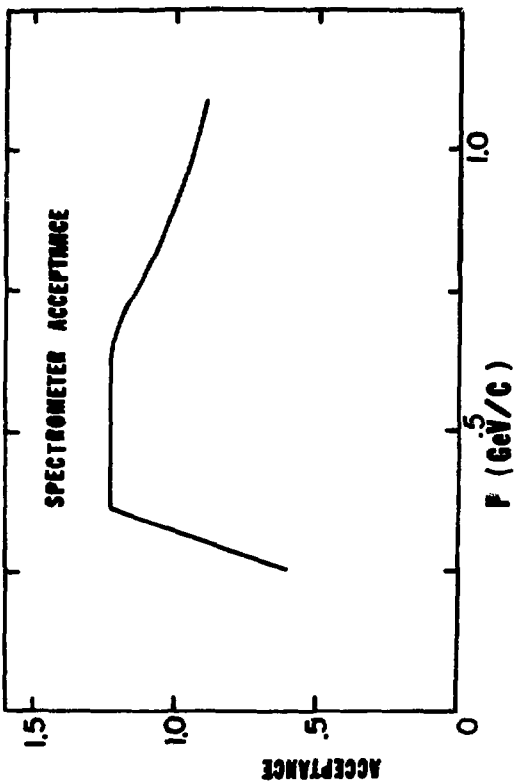

Figure 9

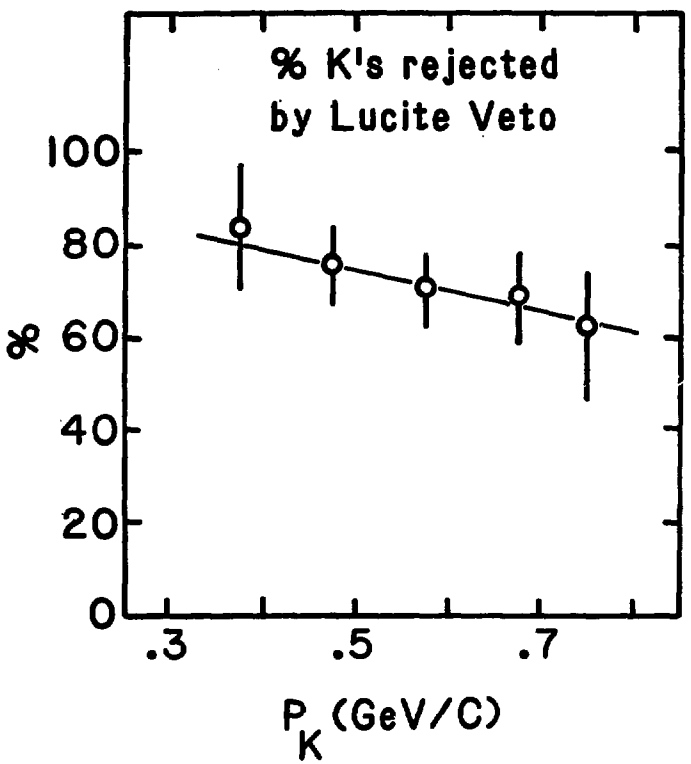

Figure 10

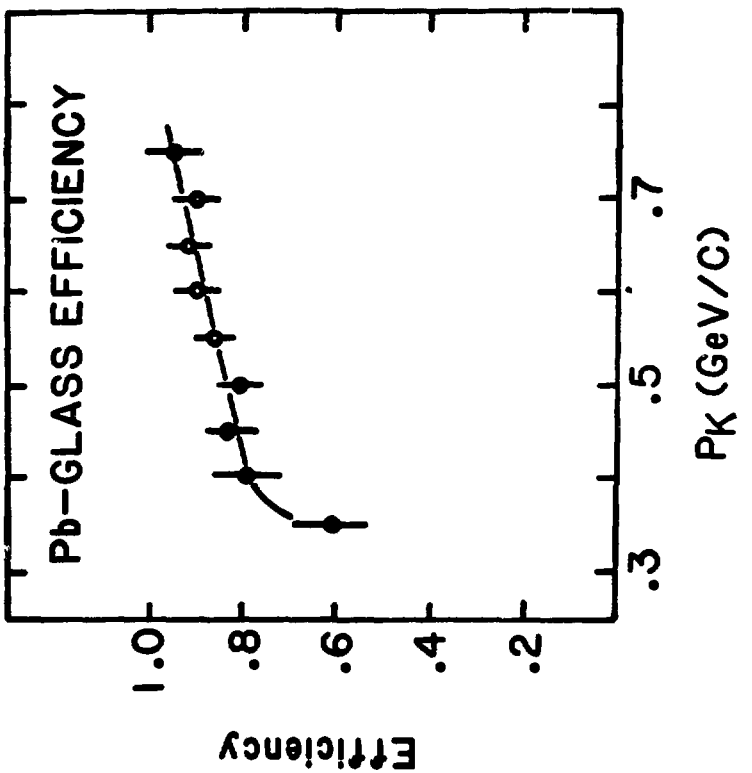

Figure 11

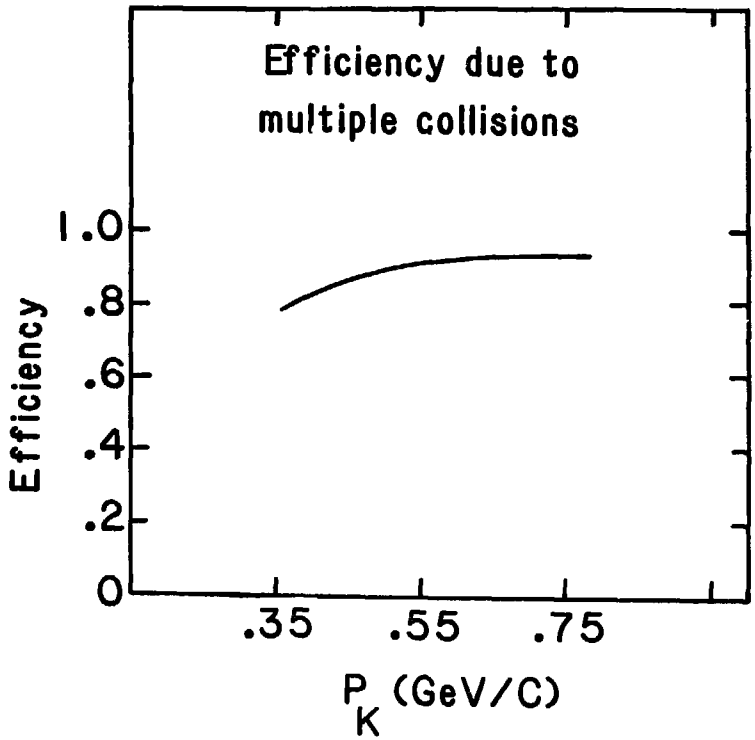
Efficiency due to
multiple collisions
Efficiency
1.0
.8
.6
.4
.2
0
.35
.55
.75
P_K (GeV/C)

Figure 12

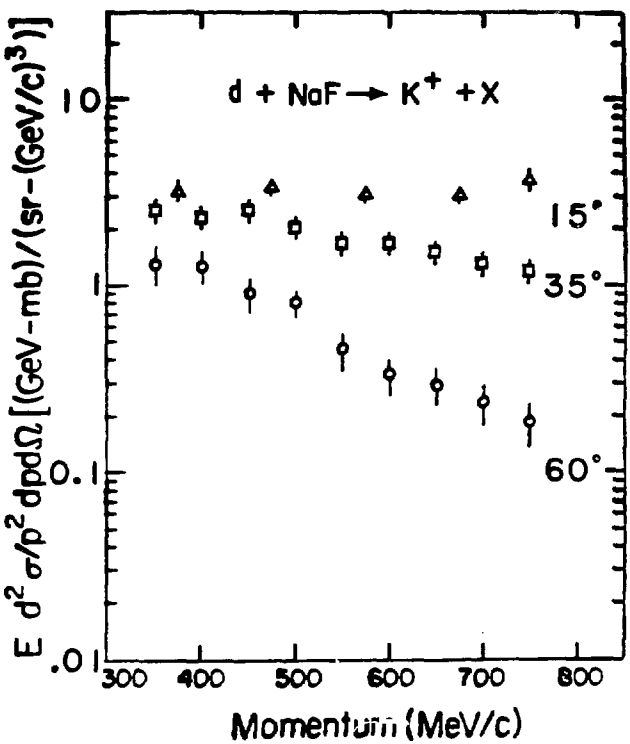
d + NaF → K+ +X
15°
35°
60°
E d²σ/p² dpdΩ [(GeV-mb)/(sr-(GeV/c)³)]
10
1
0.1
.01
300
400
500
600
700
800
Momentum (MeV/c)

Figure 13

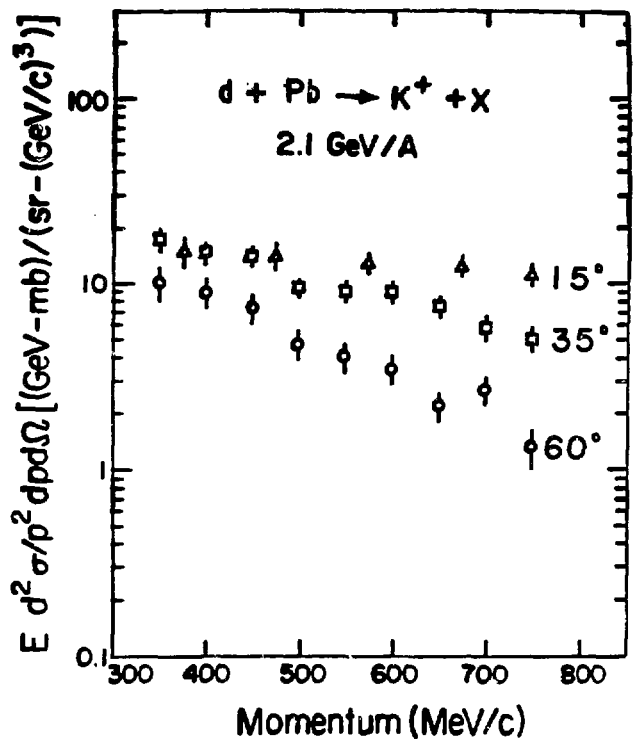
d + Pb → K+ + X
2.1 GeV/A
15°
35°
60°
E d²σ/p² dpdΩ [(GeV-mb)/(sr-(GeV/c)³)]
100
10
1
0.1
300
400
500
600
700
800
Momentum (MeV/c)

Figure 14

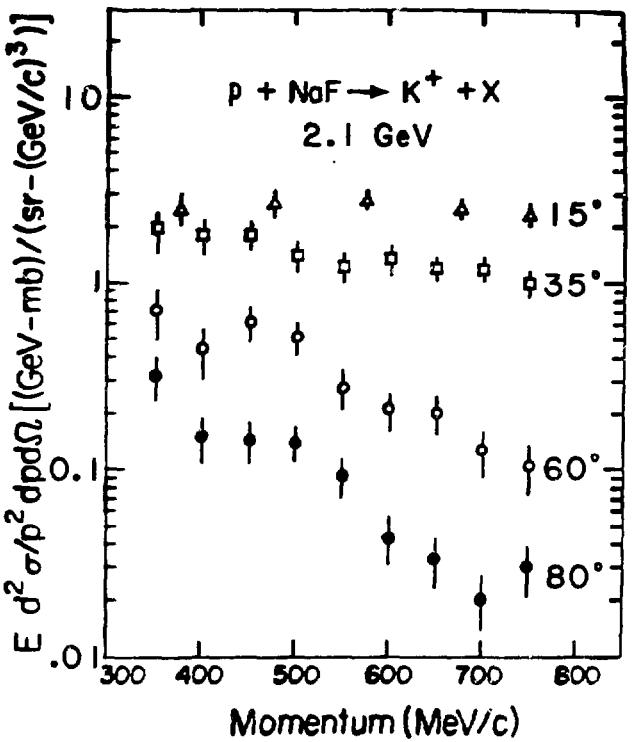
p + NaF → K+ + X
2.1 GeV
15°
35°
60°
80°
E d²σ/p²dpdΩ [(GeV-mb)/(sr-(GeV/c)³)]
10
1
0.1
.01
300
400
500
600
700
800
Momentum (MeV/c)

Figure 15

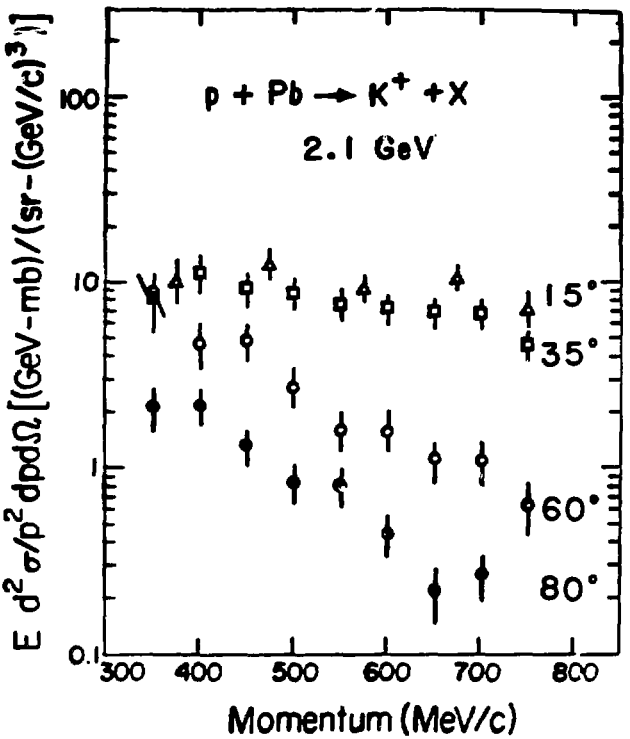
p + Pb → K+ + X
2.1 GeV
15°
35°
60°
80°
E d²σ/p²dpdΩ [(GeV-mb)/(sr-(GeV/c)³)]
100
10
1
0.1
300
400
500
600
700
800
Momentum (MeV/c)

Figure 16

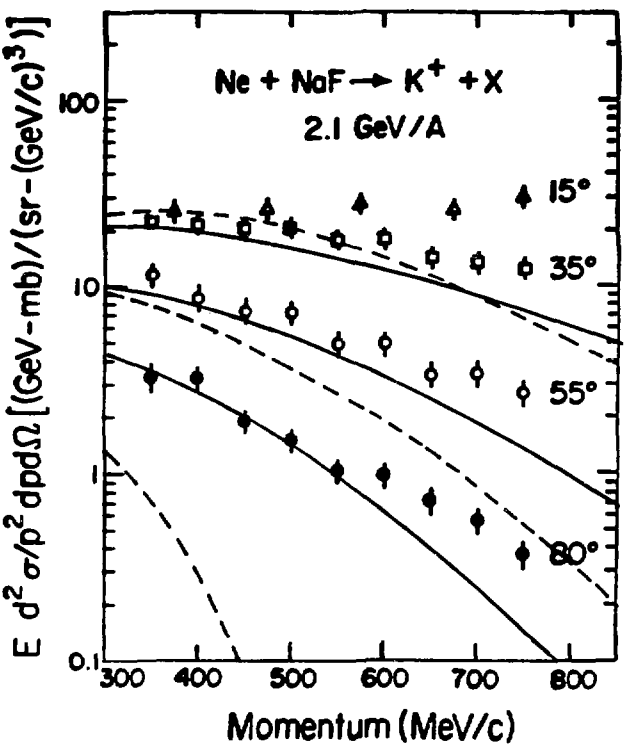
Ne + NaF → K+ + X
2.1 GeV/A
15°
35°
55°
80°
E d²σ/p²dpdΩ [(GeV-mb)/(sr-(GeV/c)³)]
100
10
1
0.1
300
400
500
600
700
800
Momentum (MeV/c)

Figure 17

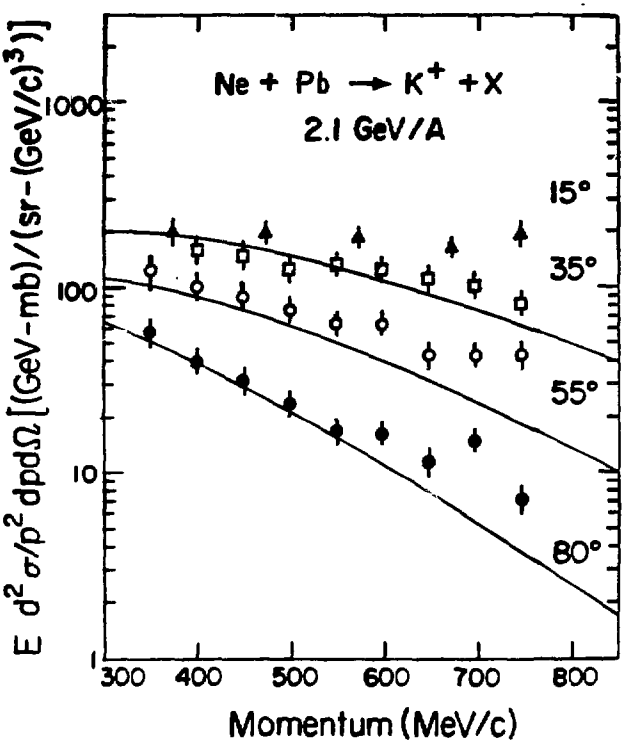
Ne + Pb → K+ + X
2.1 GeV/A
15°
35°
55°
80°
E d²σ/p² dpdΩ [(GeV-mb)/(sr-(GeV/c)³)]
1000
100
10
1
300
400
500
600
700
800
Momentum (MeV/c)

Figure 18

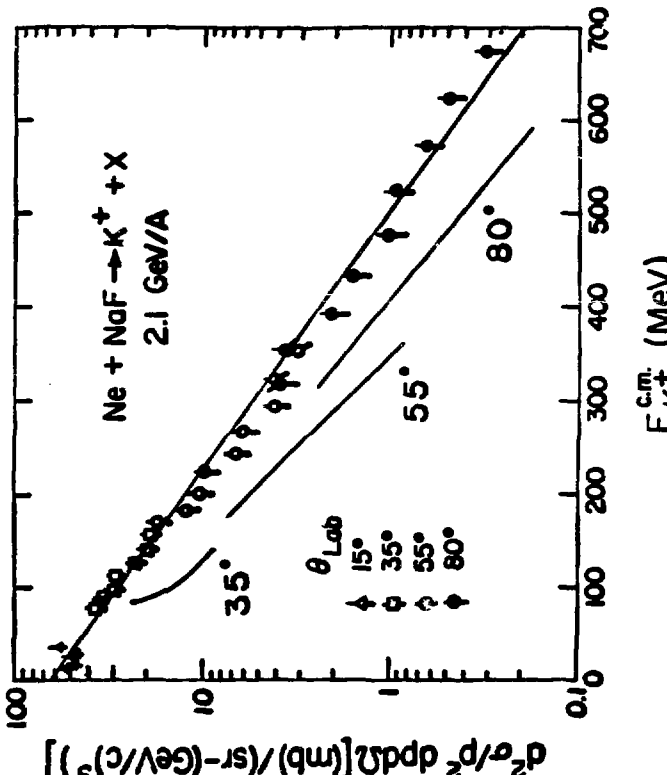
Ne + NaF → K+ + X
2.1 GeV/A
35°
55°
80°
θLab
15°
35°
55°
80°
d²σ/p² dpdΩ [(mb)/(sr-(GeV/c)³)]
E c.m. K+ (MeV)
100
10
1
0.1
0
100
200
300
400
500
600
700

Figure 19

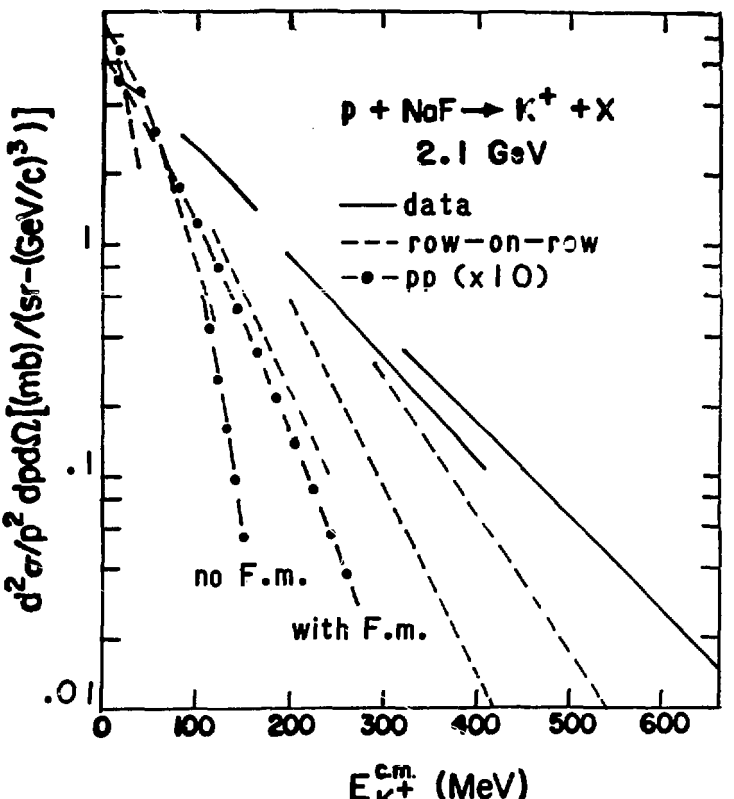
p + NaF → K+ + X
2.1 GeV
data
row-on-row
pp (x 10)
no F.m.
with F.m.
d²σ/p² dpdΩ [(mb)/(sr-(GeV/c)³)]
1
.1
.01
0
100
200
300
400
500
600
E c.m. K+ (MeV)

Figure 20

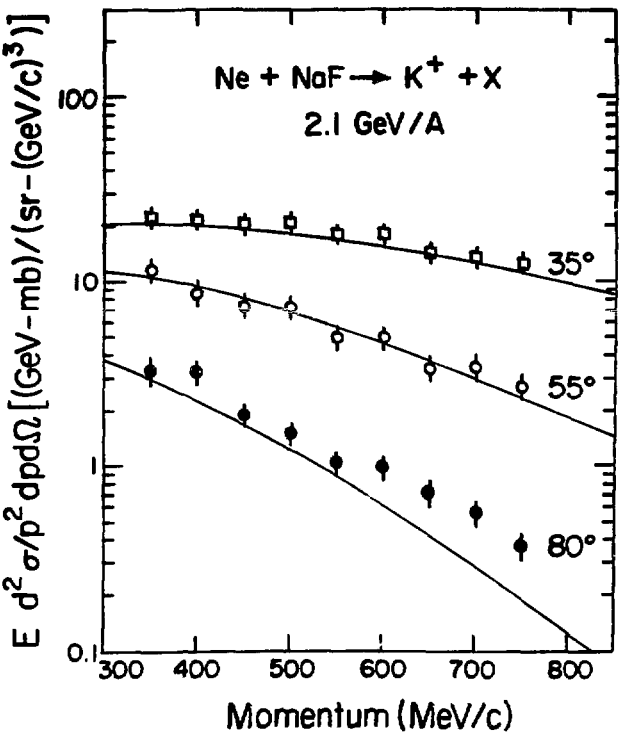
Ne + NaF → K+ + X
2.1 GeV/A
35°
55°
80°
E d²σ/p² dpdΩ [(GeV-mb)/(sr-(GeV/c)³)]
100
10
1
0.1
300
400
500
600
700
800
Momentum (MeV/c)

Figure 21

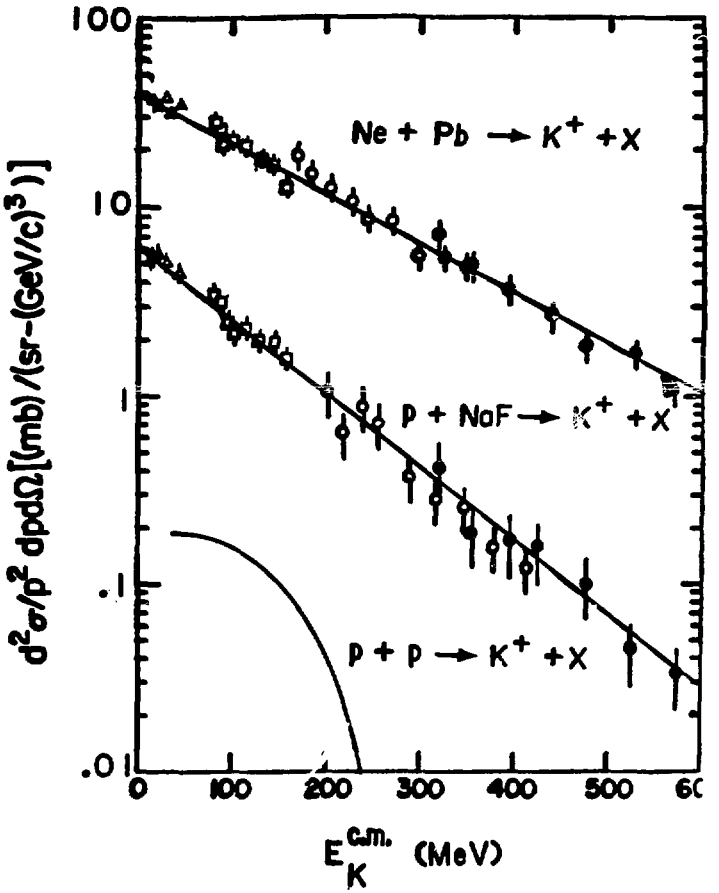
100
10
1
.1
.01
0
100
200
300
400
500
60
Ne + Pb → K+ + X
p + NaF → K+ + X
p + p → K+ + X
d²σ/p² dpdΩ[(mb)/(sr-(GeV/c)³)]
E_K^c.m. (MeV)

Figure 22

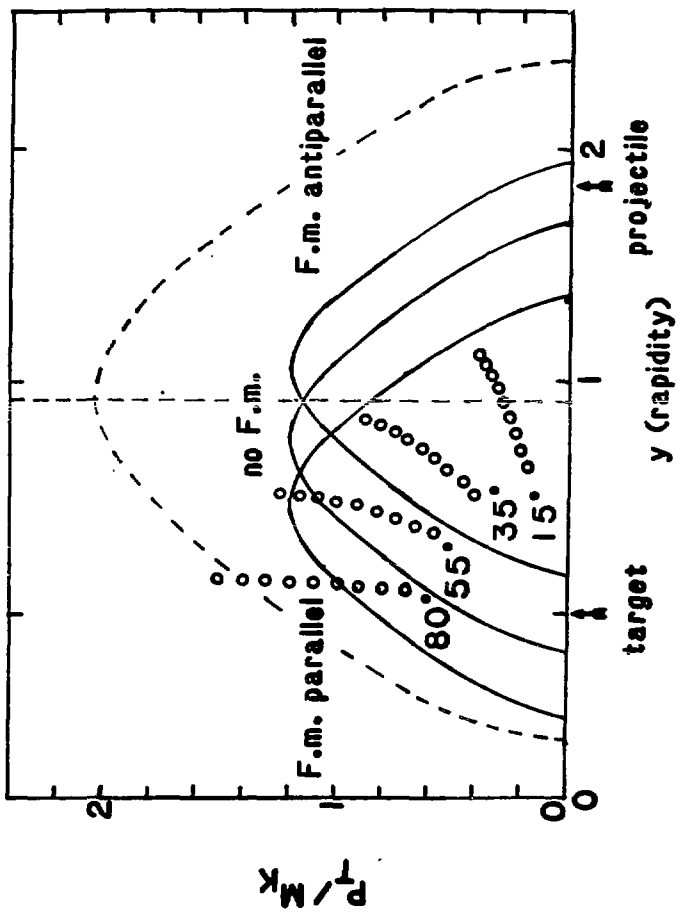
F.m. antiparallel
no F.m.
F.m. parallel
80°
55°
35°
15°
target
projectile
y (rapidity)
p_T/m_K
0
1
2

Figure 23

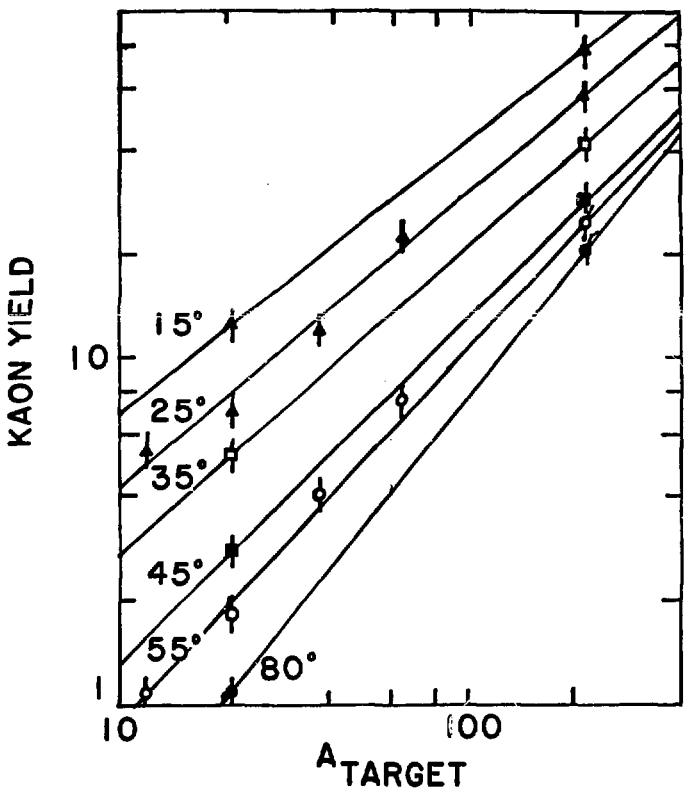

Figure 24

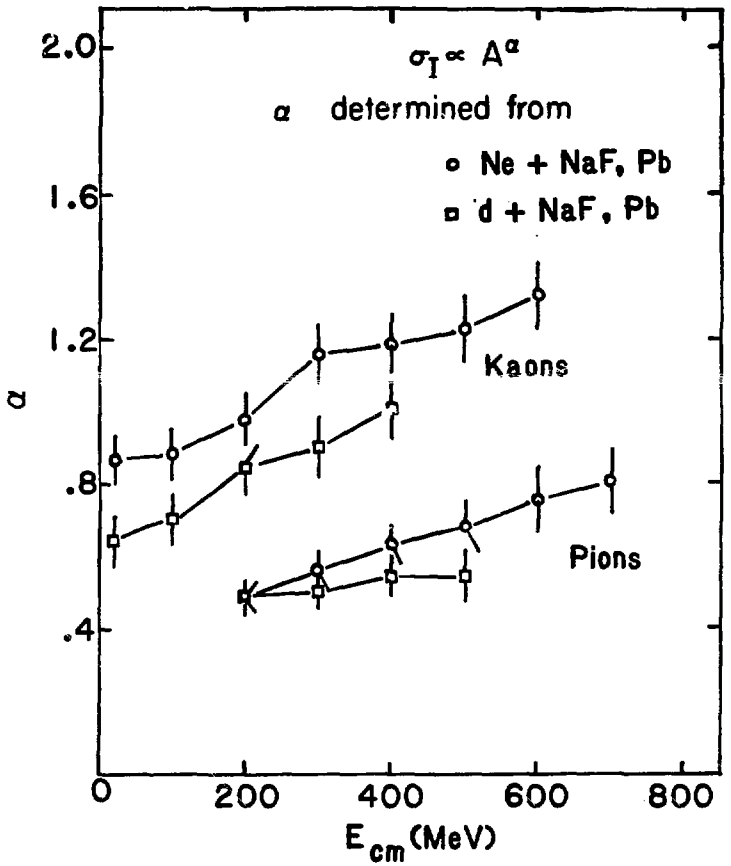
$\sigma_I \propto A^\alpha$
α determined from
o Ne + NaF, Pb
□ d + NaF, Pb
Kaons
Pions
2.0
1.6
1.2
.8
.4
α
0
200
400
600
800
E_{cm} (MeV)

Figure 25

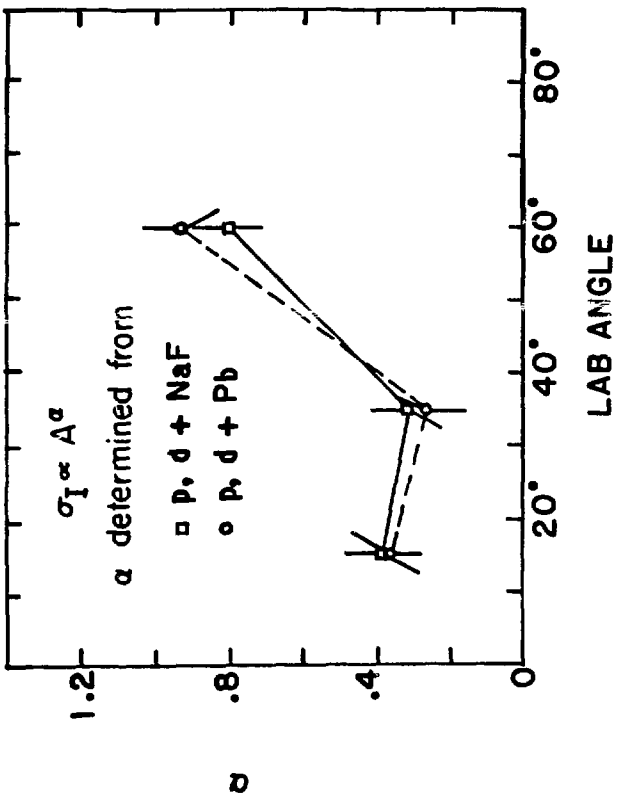
$\sigma_I \propto A^{\alpha}$
α determined from
□ p, d + NaF
○ p, d + Pb
1.2
.8
.4
0
20°
40°
60°
80°
LAB ANGLE
α

Figure 26

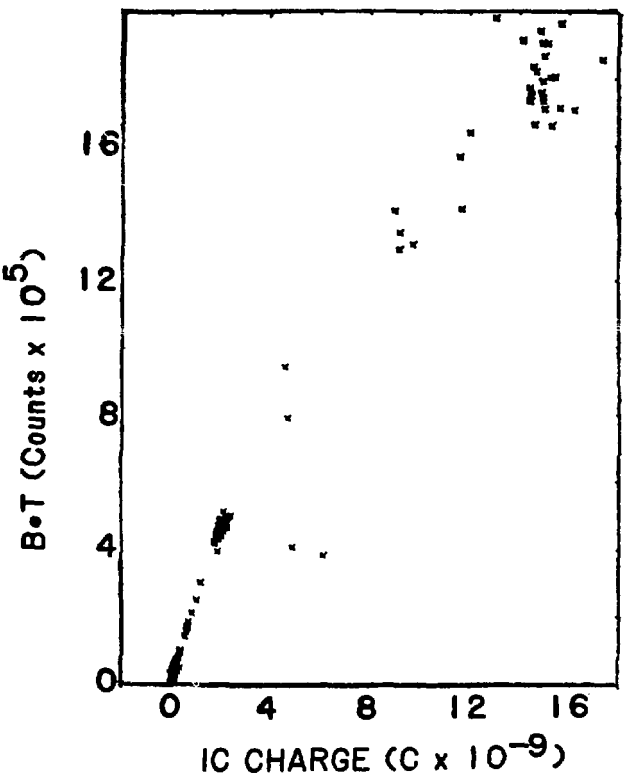

Figure 27

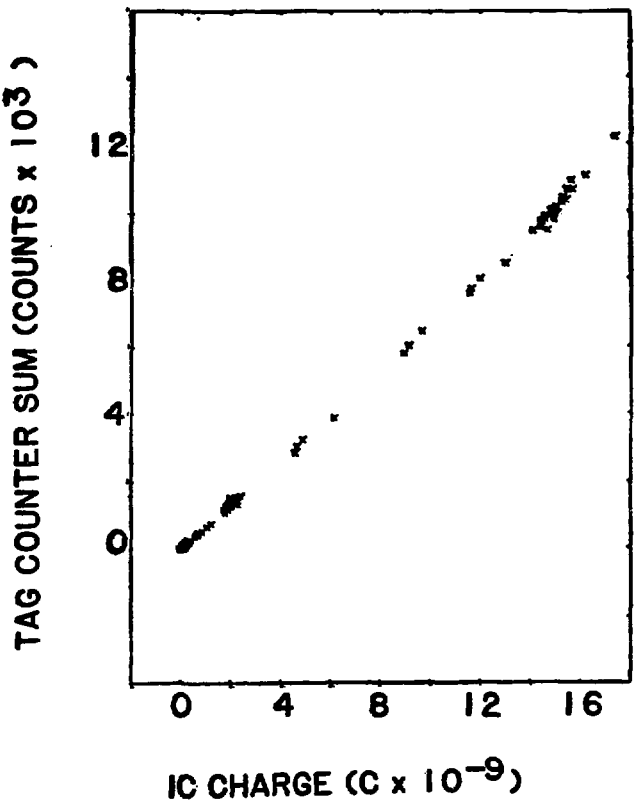

Figure 28

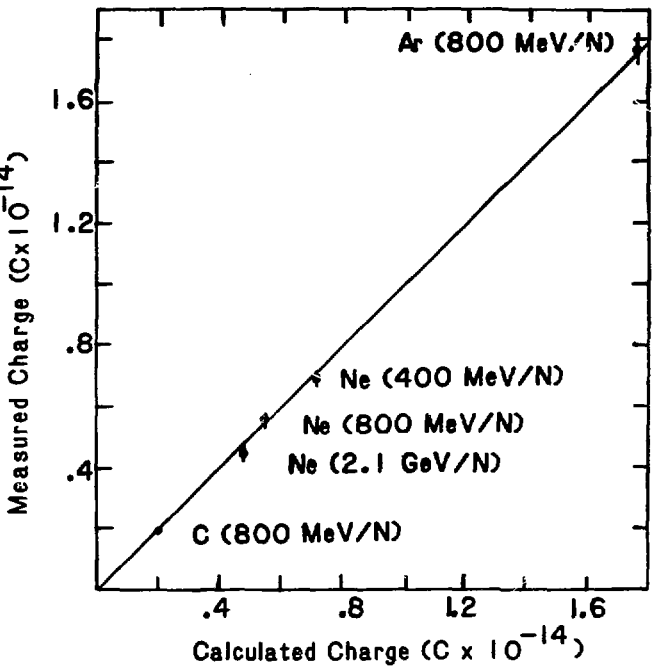
Ar (800 MeV/N)
Ne (400 MeV/N)
Ne (800 MeV/N)
Ne (2.1 GeV/N)
C (800 MeV/N)
Measured Charge (C x 10⁻¹⁴)
Calculated Charge (C x 10⁻¹⁴)
1.6
1.2
.8
.4
.4
.8
1.2
1.6

Figure 29

APPENDIX A

IONIZATION CHAMBER CALIBRATION

At the beginning of each set of runs, that is, whenever the projectile was changed, the ionization chamber, IC, was calibrated. This was was done by placing two scintillation counters directly in the beam. One counter, B, was situated immediately downstream of IC while the other counter, T, was situated near the target position. A pulse by pulse plot of the charge of the IC vs. the number of B·T coincidences was made for pulses covering a wide range of intensity. This plot for the Ne projectile is shown in Fig. 27. We see that the curve is non-linear. This is due to the fact that at ≈100,000 particles per pulse the scintillation counters begin to saturate. In Fig. 28 we plot the IC-charge vs. the sum of the tag counter counts. This curve shows that the IC itself is linear even up to very high intensities.

The quantity of interest, the IC-charge per beam particle, is given by the slope of the curve in Fig. 27. Because of the saturation of the scintillation counters, this slope is a function of beam intensity. We, therefore, calculate the true value by extrapolating to zero beam intensity. For the Ne projectile this gives a value of 4.03×10^{-15} coulombs per beam particle. In Fig. 29 we plot this point together with points obtained in a previous experiment[33] which used the same IC. These values are plotted versus values calculated from the physical parameters of the chamber. It can be seen that for all points the measured and calculated values agree to within 5%. In addition it shows that the IC follows the expected Z^2 dependence. We feel that these results indicate that we understand the chamber to within a few per cent.

Appendix B

TRIGGER ELECTRONICS

Below we describe the trigger electronics. That is, the electronics which used the signals from the various counters (G, Pb-glass, etc.) to determine if there was an acceptable event and, if so, to issue the proper gate and reset signals. For simplicity of discussion we divide the circuitry into several sections.

1. G-Counters

The fundamental trigger was determined by G1·G2·G3. In order to obtain this signal the outputs from each of the G-counter phototubes were discriminated and then applied to various coincidence circuits. In order that the timing of this signal would not depend significantly upon the velocity of the particle, its timing was designed to be determined always by the timing of the G1 pulse. The distance from the target to G1 was only 38.35 cm so that the timing difference between a particle with β=1 and β=0.3 was only 2.5 ns.

2. Dead Time

Since the "G" coincidence was common to all of the trigger, the computer dead time was incorporated in it. The output signal was "GD".

3. Pb-Glass and Lucite

The lucite and Pb-glass signals were used in conjunction with "GD" to form the additional triggers. The signals from the phototubes were amplified, discriminated, and then mixed in the case of both the lucite and the Pb-glass. The Pb-glass signal was then sent directly to the

trigger coincidence circuits, while the lucite signal was used to make two signals: $L \cdot G3$ and $\overline{L} \cdot G3$.

4. Divide Boxes

As mentioned in the text, in order to get appropriate ratios among the various triggers, they were each divided by some appropriate factor. The "GD" signal was applied to the input of a "÷ box". The box would count N of these pulses and would then transmit the Nth one and then stop. This signal was then taken in coincidence with a "GD" signal in order to maintain the original "GD" timing. There were then three outputs from this coincidence. One went to the appropriate trigger. A second went to reset the divide box so that it would start counting again. The third went to the next "÷ box". By so cascading four "÷ boxes" we could obtain four signals divided by factors from 1 to $(16)^4$.

5. Heart of the Trigger Logic

The heart of the trigger logic was a set of four coincidence circuits and an "OR" circuit. By use of the coincidence circuits the various triggers (G, $G \cdot L$, etc.) were formed. These were then or'd, and the resulting output was sent to the computer indicating that an event was to be processed. In addition, this pulse was taken in coincidence with either G1 or G3 to form the various gates and strobes needed for the pattern units, ADC's, TDC's and wire chambers.

6. Wire Chambers

When a particle traversed one of the wire chambers a "fast-out" signal was generated. This signal was then strobed with either the $G1 \cdot$trigger signal or the $G3 \cdot$trigger depending on whether it was a

forward or backward chamber. If there were a coincidence then a "write gate" signal was generated which was sent back to the chamber causing the wire hit pattern information to be encoded.

APPENDIX C

CROSS SECTION TABLES

$p + NaF \quad \theta_L = 15°$

Momentun (MeV/c)	$\frac{Ed^2\sigma}{p^2 dpd\Omega}$ $\left[\frac{GeV\text{-}mb}{sr\text{-}(GeV/c)^3}\right]$
350	3.2 ± 0.8
400	2.3 ± 0.5
450	2.7 ± 0.5
500	2.7 ± 0.4
550	2.8 ± 0.4
600	2.8 ± 0.4
650	2.3 ± 0.3
700	2.9 ± 0.4
750	2.3 ± 0.3

$p + NaF \quad \theta_L = 35°$

Momentun (MeV/c)	$\frac{Ed^2\sigma}{p^2 dp d\Omega}$ $\left[\frac{GeV\text{-}mb}{sr\text{-}(GeV/c)^3}\right]$
350	1.9 ± 0.5
400	1.8 ± 0.4
450	1.8 ± 0.3
500	1.4 ± 0.2
550	1.2 ± 0.2
600	1.4 ± 0.2
650	1.2 ± 0.2
700	1.2 ± 0.2
750	1.0 ± 0.2

$p + NaF \quad \theta_L = 60°$

Momentun (MeV/c)	$\frac{Ed^2\sigma}{p^2 dp d\Omega}$ $\left[\frac{GeV\text{-}mb}{sr\text{-}(GeV/c)^3}\right]$
350	0.70 ± 0.22
400	0.43 ± 0.13
450	0.60 ± 0.13
500	0.50 ± 0.10
550	0.27 ± 0.07
600	0.21 ± 0.05
650	0.20 ± 0.05
700	0.12 ± 0.03
750	0.10 ± 0.03

$p + NaF \quad \theta_L = 80°$

Momentun (MeV/c)	$\frac{Ed^2\sigma}{p^2 dp d\Omega}$ $\left[\frac{GeV-mb}{sr-(GeV/c)^3}\right]$
350	0.31 ± 0.08
400	0.14 ± 0.04
450	0.14 ± 0.03
500	0.14 ± 0.03
550	0.09 ± 0.02
600	0.04 ± 0.01
650	0.03 ± 0.01
700	0.02 ± 0.01
750	0.03 ± 0.01

$p+Pb \quad \theta_L = 15°$

Momentun (MeV/c)	$\frac{Ed^2\sigma}{p^2 dpd\Omega}$ $\left[\frac{GeV\text{-}mb}{sr\text{-}(GeV/c)^3}\right]$
350	9 ± 5
400	12 ± 4
450	15 ± 4
500	9 ± 2
550	9 ± 2
600	9 ± 2
650	10 ± 2
700	11 ± 2
750	7 ± 2

$p+Pb \quad \theta_L = 35°$

Momentun (MeV/c)	$\frac{Ed^2\sigma}{p^2 dp d\Omega}$ $\left[\frac{GeV-mb}{sr-(GeV/c)^3}\right]$
350	8.5 ± 3.0
400	11.7 ± 2.8
450	9.6 ± 2.1
500	9.0 ± 1.7
550	7.8 ± 1.5
600	7.4 ± 1.3
650	7.1 ± 1.2
700	6.9 ± 1.2
750	4.3 ± 0.8

$p+Pb \quad \theta_L = 60°$

Momentun (MeV/c)	$\frac{Ed^2\sigma}{p^2 dpd\Omega}$ $\left[\frac{GeV-mb}{sr-(GeV/c)^3}\right]$
350	9.0 ± 2.2
400	4.8 ± 1.2
450	5.0 ± 1.0
500	2.9 ± 0.7
550	1.6 ± 0.4
600	1.6 ± 0.4
650	1.1 ± 0.3
700	1.1 ± 0.3
750	0.6 ± 0.2

$p+Pb \quad \theta_L = 80°$

Momentum (MeV/c)	$\frac{Ed^2\sigma}{p^2 dp d\Omega}$ $\left[\frac{GeV-mb}{sr-(GeV/c)^3}\right]$
350	2.5 ± 0.6
400	2.5 ± 0.5
450	1.3 ± 0.3
500	0.87 ± 0.2
550	0.82 ± 0.2
600	0.45 ± 0.1
650	0.22 ± 0.1
700	0.27 ± 0.1
750	0.07 ± 0.03

$d+NaF \quad \theta_L = 15°$

Momentun (MeV/c)	$\frac{Ed^2\sigma}{p^2 dp d\Omega}$ $\left[\frac{GeV-mb}{sr-(GeV/c)^3}\right]$
350	2.7 ± 0.6
400	2.6 ± 0.5
450	3.1 ± 0.5
500	3.6 ± 0.5
550	3.2 ± 0.4
600	2.9 ± 0.4
650	3.3 ± 0.4
700	2.8 ± 0.3
750	3.7 ± 0.4

$d+NaF \quad \theta_L = 25°$

Momentun (MeV/c)	$\frac{Ed^2\sigma}{p^2 dp d\Omega}$ $\left[\frac{GeV-mb}{sr-(GeV/c)^3}\right]$
350	2.5 ± 0.5
400	3.3 ± 0.5
450	3.3 ± 0.4
500	3.1 ± 0.4
550	2.9 ± 0.4
600	2.7 ± 0.3
650	2.8 ± 0.3
700	2.5 ± 0.3
750	2.1 ± 0.2

$d+NaF \quad \theta_L = 35°$

Momentun (MeV/c)	$\frac{Ed^2\sigma}{p^2 dp d\Omega}$ $\left[\frac{GeV\text{-}mb}{sr\text{-}(GeV/c)^3}\right]$
350	2.0 ± 0.4
400	2.2 ± 0.3
450	2.4 ± 0.3
500	2.0 ± 0.3
550	1.6 ± 0.2
600	1.7 ± 0.2
650	1.5 ± 0.2
700	1.2 ± 0.2
750	1.1 ± 0.1

$d+NaF \quad \theta_L = 60°$

Momentun (MeV/c)	$\frac{Ed^2\sigma}{p^2 dpd\Omega}$ $\left[\frac{GeV-mb}{sr-(GeV/c)^3}\right]$
350	1.08 ± 0.30
400	1.26 ± 0.26
450	0.89 ± 0.18
500	0.78 ± 0.14
550	0.44 ± 0.09
600	0.31 ± 0.07
650	0.29 ± 0.06
700	0.23 ± 0.05
750	0.18 ± 0.04

$d+Pb \quad \theta_L = 15°$

Momentun (MeV/c)	$\frac{Ed^2\sigma}{p^2 dp d\Omega}$ $\left[\frac{GeV-mb}{sr-(GeV/c)^3}\right]$
350	11 ± 3
400	17 ± 3
450	15 ± 2
500	13 ± 2
550	13 ± 2
600	13 ± 2
650	12 ± 2
700	13 ± 2
750	11 ± 1

$d+Pb \quad \theta_{\perp} = 25°$

Momentun (MeV/c)	$\frac{Ed^2\sigma}{p^2 dp d\Omega}$ $\left[\frac{GeV-mb}{sr-(GeV/c)^3}\right]$
350	18 ± 3
400	16 ± 3
450	13 ± 2
500	14 ± 2
550	11 ± 1
600	13 ± 2
650	9 ± 1
700	9 ± 1
750	9 ± 1

$d+Pb \quad \theta_L = 35°$

Momentun (MeV/c)	$\frac{Ed^2\sigma}{p^2 dpd\Omega}$ $\left[\frac{GeV\text{-}mb}{sr\text{-}(GeV/c)^3}\right]$
350	15 7 ± 2.5
400	14.9 ± 2.0
450	14.0 ± 1.8
500	9.4 ± 1.2
550	9.0 ± 1.1
600	9.0 ± 1.1
650	7.5 ± 0.9
700	5.8 ± 0.7
750	5.0 ± 0.6

$d+Pb \quad \theta_L = 80°$

Momentun (MeV/c)	$\frac{Ed^2\sigma}{p^2 dpd\Omega}$ $\left[\frac{GeV-mb}{sr-(GeV/c)^3}\right]$
350	8.6 ± 2.2
400	8.9 ± 1.8
450	7.3 ± 1.3
500	4.7 ± 0.9
550	4.0 ± 0.8
600	3.5 ± 0.6
650	2.2 ± 0.5
700	2.8 ± 0.5
750	1.3 ± 0.3

$Ne+NaF \quad \theta_L = 15°$

Momentun (MeV/c)	$\frac{Ed^2\sigma}{p^2 dp d\Omega}$ $\left[\frac{GeV\text{-}mb}{sr\text{-}(GeV/c)^3}\right]$
350	26 ± 5
400	24 ± 4
450	23 ± 4
500	29 ± 3
550	24 ± 4
600	31 ± 3
650	25 ± 3
700	25 ± 3
750	30 ± 4

$Ne+NaF \quad \theta_L = 25°$

Momentun (MeV/c)	$\frac{Ed^2\sigma}{p^2 dpd\Omega}$ $\left[\frac{GeV \cdot mb}{sr \cdot (GeV/c)^3}\right]$
350	26 ± 4
400	30 ± 4
450	24 ± 3
500	29 ± 3
550	24 ± 3
600	23 ± 3
650	21 ± 2
700	21 ± 2
750	20 ± 2

$Ne+NaF \quad \theta_L = 35°$

Momentun (MeV/c)	$\frac{Ed^2\sigma}{p^2 dpd\Omega}$ $\left[\frac{GeV-mb}{sr-(GeV/c)^3}\right]$
350	22 ± 3
400	21 ± 3
450	21 ± 2
500	21 ± 2
550	18 ± 2
600	18 ± 2
650	14 ± 2
700	13 ± 1
750	13 ± 1

$Ne+NaF \quad \theta_L = 45°$

Momentun (MeV/c)	$\frac{Ed^2\sigma}{p^2 dpd\Omega}$ $\left[\frac{GeV\text{-}mb}{sr\text{-}(GeV/c)^3}\right]$
350	19.9 ± 3.9
400	15.0 ± 2.7
450	12.2 ± 2.0
500	13.8 ± 2.0
550	10.5 ± 1.6
600	8.6 ± 1.3
650	8.4 ± 1.2
700	6.7 ± 1.0
750	6.6 ± 1.0

$Ne+NaF \quad \theta_L = 55°$

Momentun (MeV/c)	$\frac{Ed^2\sigma}{p^2 dpd\Omega}$ $\left[\frac{GeV-mb}{sr-(GeV/c)^3}\right]$
350	11.6 ± 1.9
400	8.7 ± 1.3
450	7.3 ± 1.1
500	7.1 ± 1.0
550	4.8 ± 0.7
600	4.9 ± 0.7
650	3.4 ± 0.5
700	3.4 ± 0.5
750	2.7 ± 0.4

$Ne+NaF \quad \theta_L = 80°$

Momentun (MeV/c)	$\frac{Ed^2\sigma}{p^2 dpd\Omega}$ $\left[\frac{GeV-mb}{sr-(GeV/c)^3}\right]$
350	3.28 ± 0.60
400	3.20 ± 0.49
450	1.90 ± 0.30
500	1.50 ± 0.23
550	1.03 ± 0.17
600	0.97 ± 0.15
650	0.71 ± 0.12
700	0.55 ± 0.10
750	0.37 ± 0.07

$Ne+Pb \quad \theta_L = 15°$

Momentun (MeV/c)	$\frac{Ed^2\sigma}{p^2 dpd\Omega}$ $\left[\frac{GeV\text{-}mb}{sr\cdot(GeV/c)^3}\right]$
350	253 ± 57
400	186 ± 38
450	193 ± 34
500	202 ± 32
550	168 ± 26
600	201 ± 28
650	169 ± 24
700	162 ± 23
750	197 ± 26

$Ne+Pb \quad \theta_L = 25°$

Momentun (MeV/c)	$\frac{Ed^2\sigma}{p^2 dpd\Omega}$ $\left[\frac{GeV\text{-}mb}{sr\text{-}(GeV/c)^3}\right]$
350	153 ± 29
400	210 ± 30
450	210 ± 28
500	171 ± 22
550	156 ± 20
600	159 ± 19
650	135 ± 16
700	137 ± 16
750	133 ± 16

$Ne+Pb \quad \theta_L = 35°$

Momentun (MeV/c)	$\frac{Ed^2\sigma}{p^2 dpd\Omega}$ $\left[\frac{GeV-mb}{sr-(GeV/c)^3}\right]$
350	251 ± 38
400	166 ± 24
450	153 ± 20
500	126 ± 16
550	135 ± 17
600	129 ± 16
650	112 ± 14
700	107 ± 13
750	83 ± 10

$Ne+Pb \quad \theta_L = 45°$

Momentun (MeV/c)	$\frac{Ed^2\sigma}{p^2 dp d\Omega}$ $\left[\frac{GeV\text{-}mb}{sr\text{-}(GeV/c)^3}\right]$
350	146 ± 24
400	116 ± 17
450	117 ± 16
500	90 ± 12
550	86 ± 11
600	74 ± 9
650	63 ± 8
700	68 ± 8
750	78 ± 9

$Ne+Pb \quad \theta_L = 55°$

Momentun (MeV/c)	$\frac{Ed^2\sigma}{p^2 dpd\Omega}$ $\left[\frac{GeV-mb}{sr-(GeV/c)^3}\right]$
350	128 ± 22
400	102 ± 16
450	90 ± 13
500	76 ± 11
550	64 ± 9
600	64 ± 9
650	43 ± 6
700	43 ± 6
750	44 ± 6

$Ne+Pb \quad \theta_L = 80°$

Momentun (MeV/c)	$\frac{Ed^2\sigma}{p^2 dp d\Omega}$ $\left[\frac{GeV \cdot mb}{sr \cdot (GeV/c)^3}\right]$
350	59 ± 9
400	40 ± 6
450	32 ± 5
500	24 ± 3
550	17 ± 3
600	16 ± 2
650	11 ± 2
700	15 ± 2
750	7 ± 1